

On the Lagrangian-Eulerian Coupling in the Immersed Finite Element/Difference Method

Jae H. Lee^{1,2} and Boyce E. Griffith^{3,4,5,6}

¹Department of Mechanical Engineering, Johns Hopkins University, Baltimore, MD, USA

²Institute for Computational Medicine, Johns Hopkins University, Baltimore, MD, USA

³Departments of Mathematics, Applied Physical Sciences, and Biomedical Engineering,
University of North Carolina, Chapel Hill, NC, USA

⁴Carolina Center for Interdisciplinary Applied Mathematics, University of North Carolina,
Chapel Hill, NC, USA

⁵Computational Medicine Program, University of North Carolina, Chapel Hill, NC, USA

⁶McAllister Heart Institute, University of North Carolina, Chapel Hill, NC, USA

jaeholee@jhu.edu

Abstract

The immersed boundary (IB) method is a non-body conforming approach to fluid-structure interaction (FSI) that uses an Eulerian description of the momentum, viscosity, and incompressibility of a coupled fluid-structure system and a Lagrangian description of the deformations, stresses, and resultant forces of the immersed structure. Integral transforms with Dirac delta function kernels couple Eulerian and Lagrangian variables. In practice, discretizations of these integral transforms use regularized delta function kernels, and although a number of different types of regularized delta functions have been proposed, there has been limited prior work to investigate the impact of the choice of kernel function on the accuracy of the methodology. This work systematically studies the effect of the choice of regularized delta function in several fluid-structure interaction benchmark tests using the immersed finite element/difference (IFED) method, which is an extension of the IB method that uses finite element structural discretizations combined with a Cartesian grid finite difference method for the incompressible Navier-Stokes equations. Further, many IB-type methods evaluate the delta functions at the nodes of the structural mesh, and this requires the Lagrangian mesh to be relatively fine compared to the background Eulerian grid to avoid leaks. The IFED formulation offers the possibility to avoid leaks with relatively coarse structural meshes by evaluating the delta function on a denser collection of *interaction points*. This study investigates the effect of varying the relative mesh widths of the Lagrangian and Eulerian discretizations. Our results indicate that kernels satisfying a commonly imposed even-odd condition require higher resolution to achieve similar accuracy as kernels that do not satisfy this condition. We also find that narrower kernels are more robust and that a broad range of relatively coarse structural meshes can be used for shear dominated cases, but not for cases with large normal forces. Although this study is done within the context of the IFED method, the effect of different kernels could be important not just for this method, but also for other IB-type methods more generally.

Keywords: immersed finite element/difference method, fluid-structure interaction, regularized delta functions

1 Introduction

The immersed boundary (IB) method [1] is a non-body conforming approach to fluid-structure interaction (FSI) introduced by Peskin to model heart valves [2, 3]. The IB formulation uses an Eulerian description of the momentum, viscosity, and incompressibility of the coupled fluid-structure system, and it uses a Lagrangian description of the deformations, stresses, and resultant forces of the immersed structure. Integral transforms with Dirac delta function kernels couple Eulerian and Lagrangian variables. When these equations are discretized, the singular delta function is replaced by a regularized delta function. This coupling strategy eliminates the need for body-conforming discretizations and thereby facilitates models with very large structural deformations [4, 5]. The IB method and its extensions have enabled simulation studies in a broad range of applications, including cardiac dynamics [6–16], platelet adhesion [17], esophageal transport [18–20], heart development [21], insect flight [22, 23], and undulatory swimming [24–29]. However, only limited studies have examined the impact of the form of the regularized delta function on the accuracy of the methodology [1, 4, 30–33], and none of these focus on dynamic cases in the intermediate Reynolds number regime in which the IB method is broadly used in practice.

This work examines the impact of different choices of kernels on the dynamics using the immersed finite element/difference (IFED) method [4, 5], which is an extension of the IB method that uses finite element structural discretizations combined with a Cartesian grid finite difference method for the incompressible Navier-Stokes equations. Another key discretization parameter in the IFED method is the relative spacings between the Lagrangian and Eulerian mesh spacings [4]. Griffith and Luo [4] used the benchmark problem of viscous flow past a circular cylinder to demonstrate that the accuracy of the methodology depends on both the relative structural mesh spacing and the choice regularized kernel function. Although this is done within the context of this specific numerical method, the effect of different kernels also has implications for other IB-type methods.

The paper is organized as follows. The mathematical framework of the IFED method and the numerical settings that we want to optimize are described in Section 2. We perform and report results of our FSI benchmarks in Section 3, and the discussion and conclusion follow in Section 4.

2 Methods

2.1 Immersed Finite Element/Difference Method

The continuous IFED formulation considers fluid-structure system occupying a fixed three-dimensional Eulerian computational domain Ω that is partitioned into time-dependent fluid (Ω_t^f) and solid (Ω_t^s) subdomains, so that $\Omega = \Omega_t^f \cup \Omega_t^s$. Here, $\mathbf{x} = (x_1, x_2, x_3) \in \Omega$ are physical coordinates, $\mathbf{X} = (X_1, X_2, X_3) \in \Omega_0^s$ are reference coordinates attached to the structure, $\mathbf{N}(\mathbf{X})$ is the outward unit normal to $\partial\Omega_0^s$ at material position \mathbf{X} , and $\boldsymbol{\chi}(\mathbf{X}, t) \in \Omega_t^s$ is the physical position of material point \mathbf{X} at time t . The dynamics of the coupled system are described by

$$\rho \frac{D\mathbf{u}}{Dt}(\mathbf{x}, t) = -\nabla p(\mathbf{x}, t) + \mu \nabla^2 \mathbf{u}(\mathbf{x}, t) + \mathbf{f}(\mathbf{x}, t), \quad (1)$$

$$\nabla \cdot \mathbf{u}(\mathbf{x}, t) = 0, \quad (2)$$

$$\mathbf{f}(\mathbf{x}, t) = \int_{\Omega_0^s} \mathbf{F}(\mathbf{X}, t) \delta(\mathbf{x} - \boldsymbol{\chi}(\mathbf{X}, t)) d\mathbf{X}, \quad (3)$$

$$\frac{\partial \boldsymbol{\chi}}{\partial t}(\mathbf{X}, t) = \mathbf{U}(\mathbf{X}, t) = \int_{\Omega} \mathbf{u}(\mathbf{x}, t) \delta(\mathbf{x} - \boldsymbol{\chi}(\mathbf{X}, t)) d\mathbf{x} = \mathbf{u}(\boldsymbol{\chi}(\mathbf{X}, t), t), \quad (4)$$

in which $\frac{D}{Dt} = \frac{\partial}{\partial t} + \mathbf{u} \cdot \nabla$ is the material derivative, $\mathbf{U}(\mathbf{X}, t)$ is the Lagrangian velocity of the immersed structure, $\mathbf{u}(\mathbf{x}, t)$ and $p(\mathbf{x}, t)$ are the Eulerian velocity and pressure fields, $\mathbf{f}(\mathbf{x}, t)$ is the Eulerian structural force density, $\mathbf{F}(\mathbf{X}, t)$ is the Lagrangian force density, and $\delta(\mathbf{x}) = \prod_{i=1}^3 \delta(x_i)$ is the three-dimensional Dirac delta function. For simplicity, we assume a uniform mass density ρ and viscosity μ . Eq. (3) implies that the Eulerian and Lagrangian force densities are equivalent as densities, and Eq. (4) implies that the no-slip condition is satisfied along the fluid-structure interface. Note that because $\frac{\partial \boldsymbol{\chi}}{\partial t}(\mathbf{X}, t) = \mathbf{u}(\boldsymbol{\chi}(\mathbf{X}, t), t)$ and $\nabla \cdot \mathbf{u}(\mathbf{x}, t) = 0$, the immersed structure is incompressible [34].

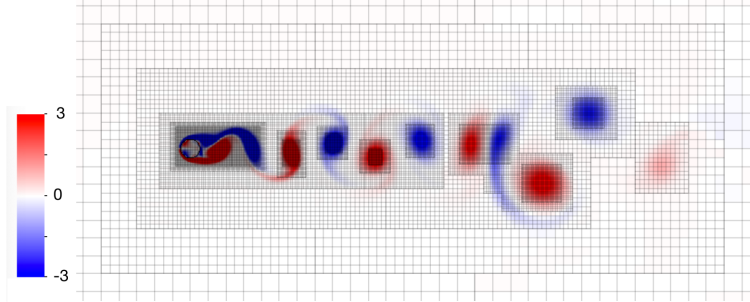


Figure 1: Vortices shed from a stationary circular cylinder at $Re = 200$. The computational domain is described by block-structured adaptively refined Cartesian grid that dynamically tracks vortices shed from the immersed structure.

In our numerical tests, we consider both rigid and elastic immersed structures. For stationary structures considered in our examples, $\mathbf{F}(\mathbf{X}, t)$ in Eq. (3) is a Lagrange multiplier for the constraint $\mathbf{U}(\mathbf{X}, t) \equiv 0$. We use a penalty formulation [35] that yields an approximate Lagrange multiplier force,

$$\mathbf{F}(\mathbf{X}, t) = \kappa(\mathbf{X} - \boldsymbol{\chi}(\mathbf{X}, t)) - \eta\mathbf{U}(\mathbf{X}, t), \quad (5)$$

in which κ is a stiffness penalty parameter and η is a body damping penalty parameter. Note that as $\kappa \rightarrow \infty$, $\boldsymbol{\chi}(\mathbf{X}, t) \rightarrow \mathbf{X}$ and $\frac{\partial \boldsymbol{\chi}}{\partial t}(\mathbf{X}, t) \rightarrow \mathbf{0}$. We include a damping term in the penalty force to reduce spurious oscillations that can occur in practice for finite κ .

We also consider immersed elastic structures in Sections 3.3, 3.4, and 3.5. In the simplest version of this methodology, the immersed structure is modeled as a viscoelastic solid, in which the viscous stresses in the solid are typically small compared to elastic stresses [4, 36–38]. In our IFED formulation, the elastic response is that of a hyperelastic material, for which the first Piola–Kirchhoff stress \mathbb{P} of the immersed structure is related to a strain-energy functional $\Psi(\mathbb{F})$ via $\mathbb{P} = \frac{\partial \Psi}{\partial \mathbb{F}}$, in which $\mathbb{F} = \partial \boldsymbol{\chi} / \partial \mathbf{X}$ is the deformation gradient tensor. The internal force $\mathbf{F}(\mathbf{X}, t)$ by the elastic structure is determined in a weak sense by satisfying

$$\int_{\Omega_0^s} \mathbf{F}(\mathbf{X}, t) \cdot \mathbf{V}(\mathbf{X}) \, d\mathbf{X} = - \int_{\Omega_0^s} \mathbb{P}(\mathbf{X}, t) : \nabla_{\mathbf{X}} \mathbf{V}(\mathbf{X}) \, d\mathbf{X} \quad (6)$$

for all smooth $\mathbf{V}(\mathbf{X})$ [4, 39]. We also use this approach as a penalty formulation to model rigid structures by treating the structure as an elastic material with a large stiffness parameter.

2.2 Eulerian and Lagrangian Discretizations

The Eulerian variables are solved on the computational domain Ω , which includes both the solid and fluid subregions, and this domain is described using a block-structured locally refined Cartesian grids consisting of nested levels of Cartesian grid patches [7]. This allows high spatial resolution to be deployed dynamically near fluid-structure interfaces and near flow features that are identified by feature detection criteria (e.g. local magnitude of the vorticity) for enhanced spatial resolution. Figure 1 provides an example of the adaptive mesh refinement in the test case of flow past a cylinder. We use a second-order accurate staggered-grid discretization [40, 41] of the incompressible Navier-Stokes that includes a version of the piecewise parabolic method (PPM) [42] to approximate the convective term.

The Lagrangian variables are solved on the immersed structure, which is discretized with \mathcal{C}^0 finite elements as described in Griffith and Luo [4]. Briefly, we construct a triangulation, \mathcal{T}^h , with m nodes, in which we define the $3m$ -dimensional vector-valued approximation space as $X^h \subset H^1(\mathcal{T}^h)^3$. We then define the standard primitive, $\{\phi_\ell\}$, nodally interpolating finite element basis of X^h . We track deformation, velocity,

and force at the nodes and use the same shape functions for each component, which can be written as

$$\boldsymbol{\chi}_h(\mathbf{X}, t) = \sum_{\ell=1}^m \boldsymbol{\chi}_\ell(t) \phi_\ell(\mathbf{X}), \quad (7)$$

$$\mathbf{U}_h(\mathbf{X}, t) = \sum_{\ell=1}^m \mathbf{U}_\ell(t) \phi_\ell(\mathbf{X}), \text{ and} \quad (8)$$

$$\mathbf{F}_h(\mathbf{X}, t) = \sum_{\ell=1}^m \mathbf{F}_\ell(t) \phi_\ell(\mathbf{X}). \quad (9)$$

Herein, we drop the subscript “ h ” from the numerical approximations to the Lagrangian variables to simplify notation.

2.3 Lagrangian-Eulerian Coupling

As briefly described in Section 1, the coupling between Eulerian and Lagrangian variables is mediated by integral transforms with delta function kernels as shown in Eq. (3) and (4). The discrete IFED coupling operators use *interaction points* that are generally chosen to be distinct from the structural mesh nodes. The interaction points are constructed by quadrature rules on the interior of the elements. In principle, this allows us to use a relatively coarser Lagrangian mesh (e.g. $M_{\text{FAC}} > 1$) and still obtain a “watertight” discretization. To approximate $\mathbf{f} = (f_1, f_2, f_3)$ in Eq. (3) on the Cartesian grid, we construct a Gaussian quadrature rule with N^e quadrature (or interaction) points $\mathbf{X}_Q^e \in K^e$ and weights w_Q^e , $Q = 1, \dots, N^e$ for each element $K^e \in \mathcal{T}^h$. Then f_1 , f_2 , and f_3 on the faces of the Cartesian grid cells are computed as [4]

$$(f_1)_{i-\frac{1}{2},j,k} = \sum_{K^e \in \mathcal{T}^h} \sum_{Q=1}^{N^e} F_1(\mathbf{X}_Q^e, t) \delta_h(\mathbf{x}_{i-\frac{1}{2},j,k} - \boldsymbol{\chi}(\mathbf{X}_Q^e, t)) w_Q^e, \quad (10)$$

$$(f_2)_{i,j-\frac{1}{2},k} = \sum_{K^e \in \mathcal{T}^h} \sum_{Q=1}^{N^e} F_2(\mathbf{X}_Q^e, t) \delta_h(\mathbf{x}_{i,j-\frac{1}{2},k} - \boldsymbol{\chi}(\mathbf{X}_Q^e, t)) w_Q^e, \quad (11)$$

$$(f_3)_{i,j,k-\frac{1}{2}} = \sum_{K^e \in \mathcal{T}^h} \sum_{Q=1}^{N^e} F_3(\mathbf{X}_Q^e, t) \delta_h(\mathbf{x}_{i,j,k-\frac{1}{2}} - \boldsymbol{\chi}(\mathbf{X}_Q^e, t)) w_Q^e, \quad (12)$$

in which $\mathbf{F}(\mathbf{X}, t) = (F_1(\mathbf{X}, t), F_2(\mathbf{X}, t), F_3(\mathbf{X}, t))$ are the Lagrangian force densities. We use the notation from Griffith and Luo [4] to re-write this as

$$\mathbf{f}(\mathbf{x}, t) = \mathcal{S}[\boldsymbol{\chi}(\cdot, t)] \mathbf{F}(\mathbf{X}, t), \quad (13)$$

in which $\mathcal{S}[\boldsymbol{\chi}(\cdot, t)]$ is the force-prolongation operator. Similarly, the velocity of the structure, $\frac{\partial \boldsymbol{\chi}}{\partial t}(\mathbf{X}, t)$ in Eq. (4), can be approximated by using the Cartesian grid velocity $\mathbf{u}(\mathbf{x}, t)$,

$$\frac{\partial \boldsymbol{\chi}}{\partial t}(\mathbf{X}, t) = \mathcal{J}[\boldsymbol{\chi}(\cdot, t)] \mathbf{u}(\mathbf{x}, t), \quad (14)$$

in which $\mathcal{J}[\boldsymbol{\chi}(\cdot, t)]$ is the velocity-restriction operator that is constructed to satisfy the adjoint condition, $\mathcal{J} = \mathcal{S}^*$ [4]. It is clear that the coupling operators \mathcal{S} and \mathcal{J} not only depend on the spatial discretization but also are constructed using the regularized delta function kernel, δ_h , and thus the choice of the kernel can affect the accuracy of the results.

2.4 Regularized Delta Functions

In our computations, we use a regularized delta function $\delta_h(\mathbf{x})$ in our discrete approximations to the integral transforms in Eq. (3) and (4). Following Peskin [1], we construct the three-dimensional regularized delta function as the tensor product of one-dimensional delta functions, $\delta_h(\mathbf{x}) = \prod_{i=1}^3 \delta_h(x_i)$, and the one-dimensional regularized delta function is defined in terms of a basic kernel function via $\delta_h(x) = \frac{1}{h} \varphi\left(\frac{x}{h}\right)$.

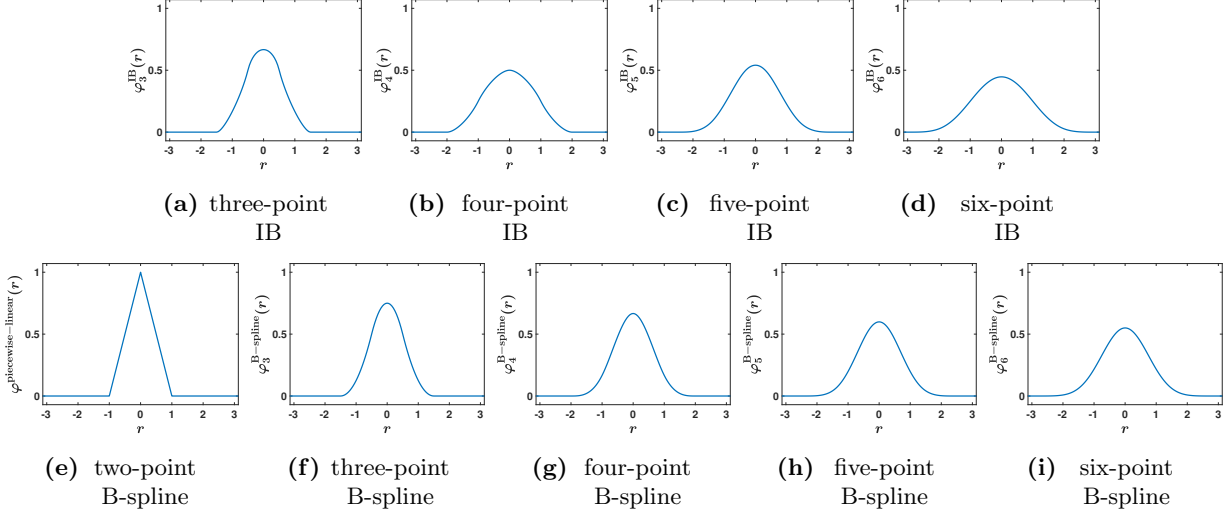


Figure 2: Selected choices of regularized delta functions. One family of kernel functions is determined by imposing some or all of the conditions described by Peskin [1], and they present different properties depending on which of the moment conditions are satisfied. We can also consider B-spline kernels that are constructed by recursive convolution against piecewise-constant kernels.

Here, $\varphi(r)$ is continuous for all r and zero outside of the radius of support. Figure 2 shows different regularized delta functions considered in this study. One-dimensional kernel functions introduced by Peskin impose some or all of the following conditions [1]:

$$\text{zeroth moment: } \sum_j \varphi(r-j) = 1; \quad (15)$$

$$\text{even-odd: } \sum_{j \text{ even}} \varphi(r-j) = \sum_{j \text{ odd}} \varphi(r-j) = \frac{1}{2}; \quad (16)$$

$$\text{first moment: } \sum_j (r-j) \varphi(r-j) = 0; \quad (17)$$

$$\text{second moment: } \sum_j (r-j)^2 \varphi(r-j) = K, \text{ for some constant } K. \quad (18)$$

The zeroth moment condition implies total forces are equivalent in discretized Lagrangian or Eulerian form when δ_h is used for force spreading [1]. The even-odd condition is designed to avoid the “checkerboard” instability in a collocated-grid fluid solver and thereby to suppress spurious high-frequency modes [1, 30, 32, 33, 41]. Note that the even-odd condition implies the zeroth moment condition. The first moment condition implies the conservation of total torque. Along with the zeroth moment condition, it guarantees second-order accuracy in interpolating smooth functions [1]. If a kernel function satisfies Eq (18) with $K = 0$, then the second moment condition implies that the kernel achieves higher order accuracy in interpolating smooth fields. It is also possible to use the higher-order moment condition with $K \neq 0$, which can be used to impose higher continuity order on the kernel function [32]. Peskin also postulated a sum-of-squares condition,

$$\sum_j (\varphi(r-j))^2 = C, \text{ for some constant } C, \quad (19)$$

which is a weak version of a grid translational invariance property [1].

At present, the kernel functions most commonly used with the IB method appear to be the IB kernels (Figures 2a-2d). The three-point IB kernel is constructed by satisfying the zeroth and first moment conditions as well as the sum-of-squares condition, but not the even-odd condition. The five-point IB kernel satisfies

Kernel	Even-Odd	Zeroth Moment	First Moment	Second Moment	Third Moment	Fourth Moment	Fifth Moment	Sum of Squares
Piecewise-linear	×	✓	✓	×	×	×	×	×
IB (3-point)	×	✓	✓	×	×	×	×	$\frac{1}{2}$
IB (4-point)	✓	✓	✓	×	×	×	×	$\frac{3}{8}$
IB (5-point)	×	✓	✓	$\frac{38}{60} - \frac{\sqrt{69}}{60}$	≈ 0	×	×	≈ 0.393
IB (6-point)	✓	✓	✓	$\frac{59}{60} - \frac{\sqrt{29}}{20}$	≈ 0	×	×	≈ 0.326
B-spline (3-point)	×	✓	✓	$\frac{1}{4}$	×	×	×	×
B-spline (4-point)	×	✓	✓	$\frac{1}{3}$	0	×	×	×
B-spline (5-point)	×	✓	✓	≈ 0.417	≈ 0	≈ 0.479	×	×
B-spline (6-point)	×	✓	✓	≈ 0.500	≈ 0	≈ 0.700	0	×

Table 1: Selected choices of regularized delta functions with properties and moment conditions that are satisfied. In the higher moment columns (second–fifth moment), the value of K that satisfies the given moment condition is given.

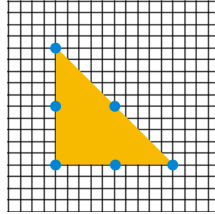


Figure 3: Description of M_{FAC} , which is the ratio between background Cartesian grid spacing and finite element node spacing. In the case shown here, there are about five Cartesian grid cells between two finite element nodes for a second-order triangular (\mathcal{P}^2) element, so we say that $M_{\text{FAC}} \approx 5$.

the same conditions as the three-point function along with second and third moment conditions. The four-point IB kernel is constructed by satisfying the even-odd condition (which also implies the zeroth moment condition) and first moment conditions as well as the sum-of-squares condition. The six-point IB kernel satisfies the same conditions as the four-point function along with second and third moment conditions.

This study also considers the performance of B-spline kernels (Figures 2f-2i), which are recursively constructed by convolution against zeroth-order B-spline kernels (equivalent to piecewise-constant kernel):

$$\varphi_n^{\text{B-spline}}(r) = \varphi_{n-1}^{\text{B-spline}}(r) * \varphi_0^{\text{B-spline}}(r) = \int_{-\infty}^{\infty} \varphi_{n-1}^{\text{B-spline}}(r-s) \varphi_0^{\text{B-spline}}(s) ds. \quad (20)$$

An n^{th} -order B-spline satisfies up to n^{th} moment conditions but does not satisfy the even-odd condition or the approximate grid translational invariance property. Both the radius of support and the smoothness of the B-spline kernel increases with order, and the limiting function is a Gaussian [33, 43]. One advantage of using B-spline kernels is that they are piecewise polynomial and can be evaluated efficiently. Table 1 shows a summary of properties and moment conditions satisfied by the kernels that are considered in this paper.

2.5 Lagrangian Mesh Spacing

In addition to the choice of the regularized delta function kernel, the coupling strategy used in the IFED method allows us to study the impact of the interaction between the Lagrangian mesh and the Eulerian grid. We use *mesh factor*, M_{FAC} , to indicate the approximate ratio of Lagrangian element node spacing to the Eulerian grid spacing. M_{FAC} is defined here as $M_{\text{FAC}} \approx \frac{\Delta X}{E_{\text{FAC}} \Delta x}$, in which ΔX is the Lagrangian element size, Δx is the Eulerian grid spacing in each coordinate direction, and the *element factor* E_{FAC} is 1 for linear elements and 2 for quadratic elements, and reflects the fact that, e.g., nodes are approximately $\Delta X/2$ apart for quadratic elements. See Figure 3. We investigate the effect of the choice of M_{FAC} , along with the choice of the regularized delta function kernel, in the accuracy of our solutions through our FSI benchmarks.

2.6 Time Discretization

As detailed previously, we use an explicit midpoint rule for the structural deformation, a Crank-Nicolson scheme for the viscous term, and an Adams-Bashforth scheme for the convective term [4]. Each time step involves solving the time-dependent incompressible Stokes equations, one force evaluation and force spreading, and two velocity interpolations.

2.7 Stabilization method for hyperelastic material models

In the continuous IFED formulation, the immersed structure is automatically treated as incompressible because $\frac{\partial \mathbf{X}}{\partial t}(\mathbf{X}, t) = \mathbf{u}(\mathbf{X}(\mathbf{X}, t), t)$ and $\nabla \cdot \mathbf{u}(\mathbf{x}, t) = 0$. In the spatially discretized equations, exact incompressibility can be lost in the solid. We use a stabilization approach [34] that effectively reinforces the incompressibility constraint. This approach uses a splitting of the strain energy functional into isochoric and volumetric parts,

$$\Psi(\mathbb{F}) = W(\bar{\mathbb{F}}) + U(J), \quad (21)$$

in which $\bar{\mathbb{F}} = J^{-1/3}\mathbb{F}$, as is commonly done in nearly incompressible elasticity models [44]. We use the volumetric part of the strain energy as a stabilization term used to enforce the incompressibility of the elastic structures, and here we choose it to be [45]

$$U(J) = \beta(J \ln J - J + 1), \quad (22)$$

in which β is a numerical bulk modulus [34].

2.8 IBAMR

FSI simulations use the IBAMR software infrastructure, which is a distributed-memory parallel implementation of the IB method with adaptive mesh refinement (AMR) [46, 47]. IBAMR uses SAMRAI [48] for Cartesian grid discretization management, libMesh [49] for finite element discretization management, and PETSc [50] for linear solver infrastructure.

3 Fluid-Structure Interaction Benchmarks

3.1 Two-dimensional flow past cylinder

We begin by considering the widely used test of viscous incompressible flow past a stationary circular cylinder [4, 51]. We use the penalty formulation, Eq. (5), to model the cylinder, using penalty parameters κ and η determined to be approximately the largest stable values for a given time step size and Lagrangian and Eulerian mesh spacings. The cylinder has diameter $D = 1$ and is embedded in a computational domain Ω with side lengths of $L = H = 60$. Figure 4a provides a schematic diagram. We use a uniform inflow velocity boundary condition, $\mathbf{u} = (1, 0)$, on the left boundary of the computational domain along with zero normal traction and tangential velocity on the right boundary. For the top and bottom boundaries of the computational domain, we use zero normal velocity and tangential traction. The fluid has density $\rho = 1$ and viscosity $\mu = 0.005$, and the Reynolds number is $Re = \frac{\rho u_\infty D}{\mu} = 200$. We use the drag $\left(C_D = \frac{F_x}{\rho u_\infty^2 D/2}\right)$ and lift $\left(C_L = \frac{F_y}{\rho u_\infty^2 D/2}\right)$ coefficients evaluate the effect of the choice of regularized delta function or mesh factor on the computed dynamics, in which $\mathbf{F} = (F_x, F_y)$ is the net force on the cylinder and u_∞ is the characteristic flow speed (which we take to be x -component of the inflow velocity). The computational domain is discretized using a six-level locally refined grid with a refinement ratio of two between levels and an $N \times N$ coarse grid. The fine-grid Cartesian cell size is $\Delta x = H/(32N)$, and the time step size that we use here is $\Delta t = 0.1875/N$ for each resolution. Griffith and Luo [4] previously conducted an initial benchmark study with different IB delta function kernels. Figure 5 shows representative results of lift and drag coefficients using the three-point B-spline kernel. We observe that under simultaneous Lagrangian and Eulerian grid refinement, the scheme converges to the same dynamics for all values of M_{FAC} . Note that the results for different kernels also converge to the same answer. Similar results are observed for all choices of kernels and for all values of M_{FAC} .

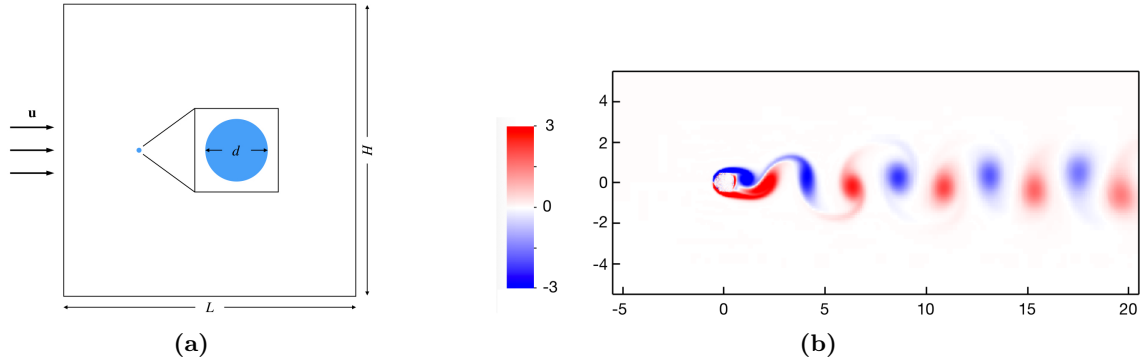


Figure 4: (a) Schematic of two-dimensional flow past a cylinder benchmark. Arrows represent the inflow boundary, where a uniform velocity boundary condition, $\mathbf{u} = (1, 0)$, is applied. Zero normal traction and tangential velocity at the outflow boundary. For the top and bottom boundaries, we use zero normal velocity and tangential traction. We choose $Re = 200$ in our tests. (b) A magnified view of the vortices shed from a stationary circular cylinder from our simulation.

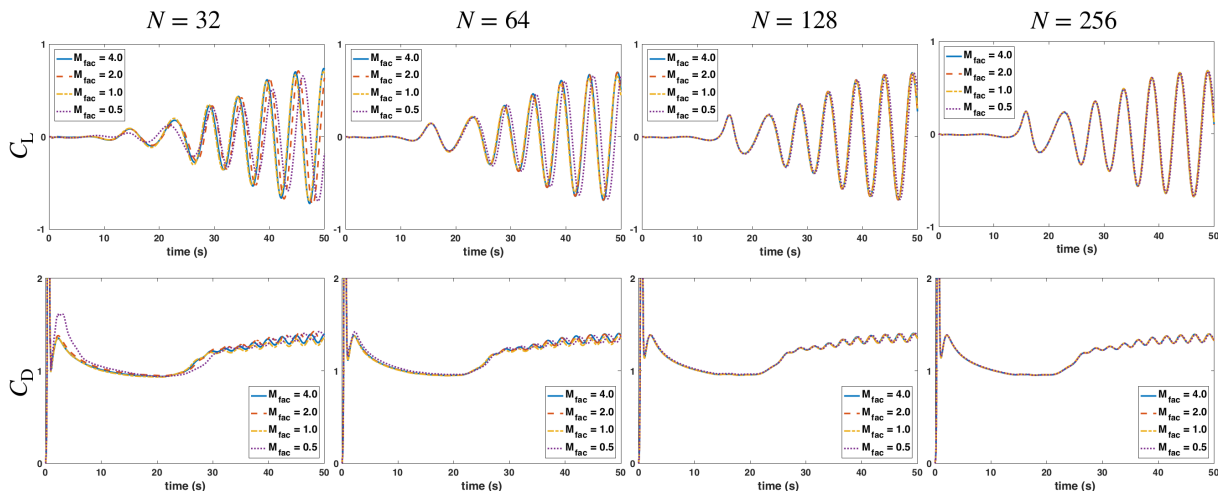


Figure 5: Representative lift (C_L) and drag (C_D) coefficients for flow past a stationary cylinder at $Re = 200$ using the three-point B-spline kernel. The computational domain Ω is discretized using a six-level locally refined grid with a refinement ratio of two between levels and an $N \times N$ coarse grid. Under simultaneous Lagrangian and Eulerian grid refinement, the scheme converges to the same dynamics for all values of M_{FAC} . Similar accuracy is observed with the other kernels except for the six-point IB kernel, which requires higher resolution to yield comparable accuracy.

Although the scheme converges under grid refinement for all choices of kernels and for all values of M_{FAC} , we observe that four- and six-point IB kernels require high grid resolution to obtain converged solutions for $M_{FAC} = 0.5$ and 1. Considering specifically the intermediate Cartesian resolution corresponding to $N = 64$, we find that some kernels show lower accuracy for some M_{FAC} values. At the same moderate resolution, the three-point IB kernel shows comparable results for $M_{FAC} \geq 1$, which agrees with the results reported by Griffith and Luo [4]. At this resolution, results for $M_{FAC} = 0.5$ are less consistent with the results for $M_{FAC} \geq 1$. Herein, we compare results at the same resolution with a broader selection of kernel functions to study which kernels give more consistent results over different values of M_{FAC} at a relatively coarse resolution. Table 2 compares lift and drag coefficients and Strouhal numbers at $N = 64$ using different kernel functions for $M_{FAC} = 0.5, 1, 2,$ and 4. These values converge to $C_L = \pm 0.67$, $C_D = 1.361 \pm 0.041$, and $St = 0.200$ under grid refinement, and we observe that the three-point IB and three- and four-point B-spline kernels with

Kernel	$M_{\text{FAC}} = 0.5$			$M_{\text{FAC}} = 1.0$			$M_{\text{FAC}} = 2.0$			$M_{\text{FAC}} = 4.0$		
	C_L	C_D	St	C_L	C_D	St	C_L	C_D	St	C_L	C_D	St
Piecewise-linear	± 0.45	1.350 ± 0.045	0.180	± 0.61	1.346 ± 0.030	0.200	± 0.69	1.389 ± 0.039	0.200	± 0.70	1.400 ± 0.042	0.200
IB (3-point)	± 0.53	1.375 ± 0.045	0.200	± 0.61	1.347 ± 0.028	0.200	± 0.66	1.357 ± 0.036	0.200	± 0.66	1.358 ± 0.036	0.200
IB (4-point)	± 0.44	1.359 ± 0.042	0.200	± 0.62	1.446 ± 0.047	0.180	± 0.64	1.347 ± 0.031	0.200	± 0.64	1.348 ± 0.031	0.200
IB (5-point)	± 0.46	1.360 ± 0.044	0.180	± 0.55	1.432 ± 0.053	0.200	± 0.64	1.346 ± 0.032	0.200	± 0.64	1.343 ± 0.033	0.200
IB (6-point)	± 0.51	1.366 ± 0.042	0.180	± 0.70	1.467 ± 0.043	0.180	± 0.63	1.332 ± 0.029	0.200	± 0.63	1.332 ± 0.029	0.200
B-spline (3-point)	± 0.51	1.354 ± 0.042	0.200	± 0.62	1.336 ± 0.032	0.200	± 0.67	1.363 ± 0.037	0.200	± 0.67	1.366 ± 0.037	0.200
B-spline (4-point)	± 0.50	1.350 ± 0.043	0.200	± 0.61	1.355 ± 0.031	0.200	± 0.66	1.357 ± 0.035	0.200	± 0.66	1.356 ± 0.035	0.200
B-spline (5-point)	± 0.49	1.358 ± 0.043	0.200	± 0.60	1.389 ± 0.040	0.200	± 0.65	1.351 ± 0.034	0.200	± 0.65	1.349 ± 0.034	0.200
B-spline (6-point)	± 0.49	1.368 ± 0.044	0.180	± 0.56	1.422 ± 0.051	0.200	± 0.64	1.346 ± 0.032	0.200	± 0.64	1.344 ± 0.032	0.200

Table 2: Comparison of lift (C_L) and drag (C_D) coefficients for flow past a stationary cylinder at an intermediate Cartesian resolution of $N = 64$ using different regularized delta functions and relative structural mesh spacing (M_{FAC}). These values converge to $C_L = \pm 0.67$, $C_D = 1.361 \pm 0.041$, $St = 0.200$ under further grid refinement. We observe that the three-point IB and three- and four-point B-spline kernels result in the highest accuracies and least variation across M_{FAC} values at $N = 64$.

$M_{\text{FAC}} > 1$ result in the highest accuracy at $N = 64$. For $M_{\text{FAC}} = 0.5$, lift and drag are less consistent with values obtained for $M_{\text{FAC}} \geq 1$. These kernels also give consistent Strouhal numbers for the values of M_{FAC} considered. Figure 6 compares lift and drag coefficients as functions of time for four representative kernels. Although Table 2 suggests that the three-point IB and three-point B-spline kernels are equally accurate, the three-point B-spline kernel yields more consistent results as we vary M_{FAC} (Figure 6). These results also show that refining the Lagrangian mesh while keeping the Eulerian grid resolution fixed generally lowers the accuracy. We find that the three-point B-spline kernel shows the least sensitivity at the coarsest grid spacings amongst the kernel functions considered in this study. Possible explanations for relatively lower accuracy and consistency from other kernels could be that the piecewise linear kernel is not sufficiently smoothing out the high-frequency errors and the larger IB and B-spline kernels are overestimating the boundary layers. We also note that the four- and six-point IB kernels satisfy the even-odd condition.

3.2 Two-dimensional channel flow

In this section, we benchmark the numerical results for two-dimensional channel flow. We consider a domain $\Omega = [0, L]^2$ with two parallel plates, with channel width D and wall width $w = 0.24D$. The exact steady-state solution is described by the plane Poiseuille equation,

$$u(y) = \frac{\chi D}{2\mu}(y - y_0) \left(1 - \frac{y - y_0}{D}\right), \quad (23)$$

in which y_0 is the height of inner wall of the lower channel plate and $\chi = \frac{2p_0}{L}$ is the pressure gradient between the inflow and the outflow. To avoid a purely grid aligned test, we consider a slanted channel. Figure 7a provides a schematic. This is done by rotating the channel walls by an angle θ , so that for every point on the walls (x, y) , we transform the y -coordinate to $y' = y + (x - \frac{L}{2}) \tan \theta$ and let (x, y') be the new coordinates for the walls. The steady-state solution is then transformed to

$$u(\eta) = \frac{\chi D}{2\mu}(\eta - \eta_0) \left(1 - \frac{\eta - \eta_0}{D}\right), \quad (24)$$

in which $\eta = -x \sin \theta + (y - y_0) \cos \theta$ and $\chi = \frac{2p_0}{L/\cos \theta + D \tan \theta}$. In our computations, we use $D = 1$, $\mu = 0.01$, $\rho = 1.0$, $L = 6D$, $p_0 = 0.2$, and $\theta = \pi/18$. The fine-grid Cartesian cell size is $\Delta x = H/(4N)$, and the time

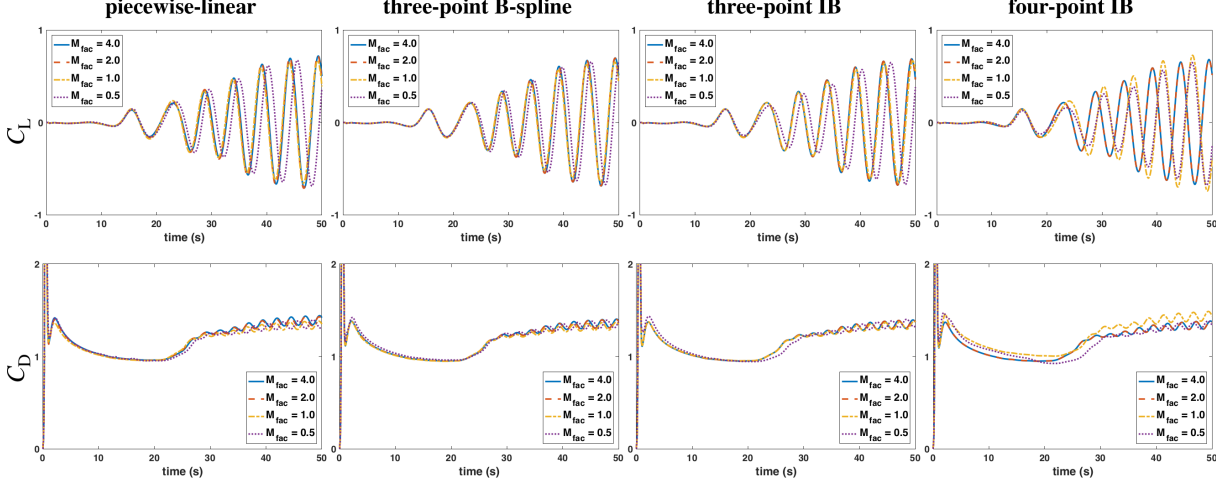


Figure 6: Representative results of lift (C_L) and drag (C_D) coefficients for flow past a stationary cylinder at $N = 64$ using four representative regularized delta functions and different relative structural mesh spacing for a fixed Eulerian grid ($M_{\text{FAC}} = 0.5, 1, 2,$ and 4).

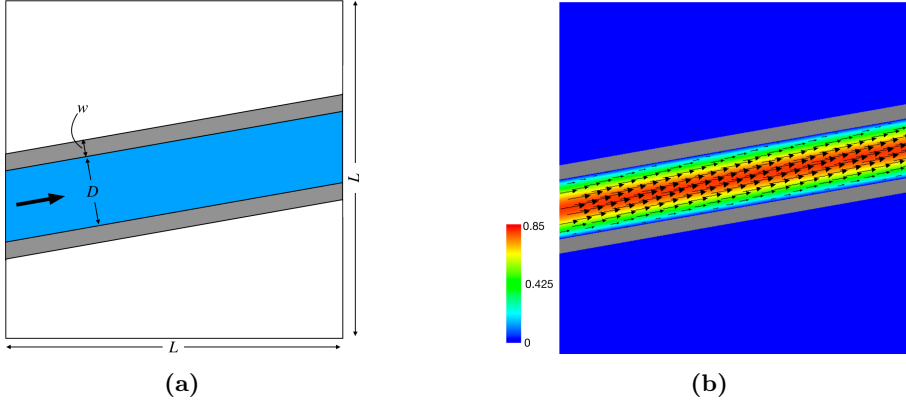


Figure 7: (a) Schematic of two-dimensional flow through a slanted channel. (b) Representative steady-state velocity solution vector field for the two-dimensional slanted channel flow benchmark. This simulation uses a three-level locally refined grid with a refinement ratio of two between levels and an $N \times N$ coarse grid with $N = 256$. The computation uses a piecewise-linear kernel and $M_{\text{FAC}} = 2.0$.

step size that we use here is $\Delta t = 0.0375/N$ for each resolution. At the inlet and outlet of the channel, the rotated analytical solution of the steady-state velocity (Eq. (24)) provides velocity boundary conditions. This benchmark tests which kernel and M_{FAC} give the best accuracy for the flow within a stationary geometry.

The channel walls are modeled as a stiff neo-Hookean material with $W_{\text{wall}} = \frac{c_{\text{wall}}}{2}(\bar{I}_1 - 3)$, in which \bar{I}_1 is the modified first invariant of the right Cauchy-Green tensor $\bar{\mathbb{C}} = \bar{\mathbb{F}}^T \bar{\mathbb{F}} = J^{-\frac{2}{3}} \mathbb{F}^T \mathbb{F}$, and $c_{\text{wall}} \propto h/\Delta t^2$ is a penalty stiffness parameter, so that the body becomes infinitely rigid as $\Delta t \rightarrow 0$. We use additional penalty body and damping forces described in Eq. (5) to enforce rigidity of the structure as well as keep it stationary. We empirically determine approximately the largest values of the penalty parameters that allow the scheme to remain stable for each kernel and grid spacing.

Figure 8 shows a convergence study using different error norms for some representative kernels with $M_{\text{FAC}} = 2.0$. These results indicate that the velocity converges at first order for all kernels. Similar convergence rates are observed for $M_{\text{FAC}} = 0.5, 1.0, 2.0,$ and 4.0 . We find that using the piecewise-linear kernel leads to the best accuracy for this test. Figure 9 shows the error plots in velocity for representative kernels for $M_{\text{FAC}} = 0.5, 1, 2,$ and 4 at $N = 128$. In all cases, we observe the general trend that the cases with

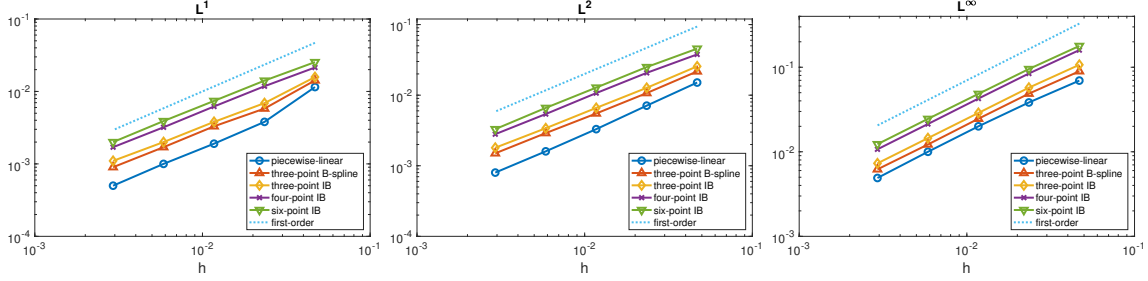


Figure 8: Representative log-log plot of different error norms in velocity with respect to the finest Eulerian mesh width h for various kernels with $M_{\text{FAC}} = 2.0$. The piecewise-linear kernel shows the smallest errors. Note that first-order convergence is obtained with all choices of kernels and for all values of M_{FAC} .

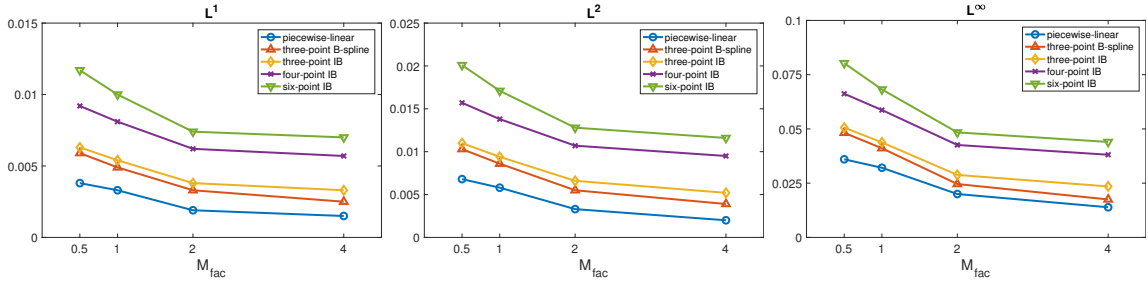


Figure 9: Plot of the error norms in velocity for values of $M_{\text{FAC}} = 0.5, 1, 2,$ and 4 at $N = 128$ for various kernels. It shows that the structural mesh that is relatively coarser than the finest background Cartesian grids yields the lowest error. The piecewise-linear kernel shows the smallest errors. Note that similar results are obtained at all resolutions with all choices of kernels.

$M_{\text{FAC}} \geq 1$, i.e. cases in which the structural mesh that is relatively coarser than the background Cartesian grids, result in better accuracy. Similar results are obtained at all resolutions with all choices of kernels. These results demonstrate that the kernels with relatively narrower support (piecewise linear, three-point IB, and three-point B-spline) and using a relatively coarser structural mesh yield the best accuracy for simulating internal flow within a stationary geometry. As in the tests reported in Section 3.1, we also observe that the scheme converges under grid refinement for all choices of kernels and for all values of M_{FAC} .

3.3 Modified Turek-Hron benchmark

Next we consider the Turek-Hron FSI benchmark of flow interacting with a flexible elastic beam mounted to a stationary circular cylinder [52]. Figure 10 shows a schematic of the setup for this benchmark. The domain length is $L = 2.5$ and height is $H = 0.41$. Note that for the actual simulation we use $L = 2.46 = 6.0H$ for the domain to obtain square Cartesian grid cells, but this change is small enough to affect the results. The fine-grid Cartesian cell size is $\Delta x = H/(4N)$, and the time step size that we use here is $\Delta t = 0.001025/N$ for each N . The circular cylinder is centered at $(0.2, 0.2)$ with radius $r = 0.05$. The elastic beam has length $l = 0.35$ and height $h = 0.02$. The left end of the beam is fixed at the cylinder. We track the position of the control point A highlighted in Figure 10b, whose initial position is at $A(0) = (0.6, 0.2)$. The boundary conditions are $u(0, y) = 1.5\bar{U} \frac{y(H-y)}{(H/2)^2}$ for $x = 0$, zero normal traction and zero tangential velocity conditions for $x = L$, and zero velocity condition for $y = 0$ and $y = H$. Notice that without the elastic beam, this problem reduces to a version of the flow past a cylinder problem. Results reported in Section 3.1 indicate that the three-point B-spline kernel provides the best accuracy at a given spatial resolution among the kernel functions considered in this study for our staggered-grid discretization [4]. Consequently, here we use the three-point B-spline kernel with $M_{\text{FAC}} = 2.0$ for the cylinder. Also note that, following the specification of the test by Turek and Hron, the immersed body is positioned asymmetrically in the y -direction to set off motion for the elastic beam.

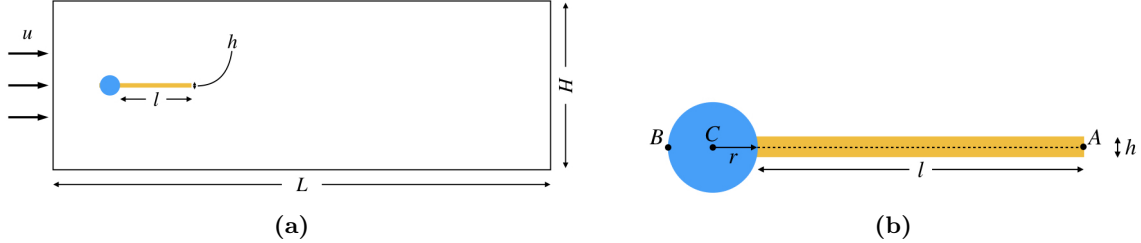


Figure 10: (a) Schematic of the Turek-Hron benchmark [52]. (b) Detail of the immersed cylinder and flexible beam.

	$M_{\text{FAC}} = 0.5$		$M_{\text{FAC}} = 1.0$		$M_{\text{FAC}} = 2.0$		$M_{\text{FAC}} = 4.0$	
N	$u_x(A) (\times 10^{-3})$	St_x	$u_x(A) (\times 10^{-3})$	St_x	$u_x(A) (\times 10^{-3})$	St_x	$u_x(A) (\times 10^{-3})$	St_x
32	-2.30 ± 2.16	10.4	-2.63 ± 2.47	10.4	-2.89 ± 2.85	10.4	-3.16 ± 3.00	10.8
64	-2.57 ± 2.44	10.8	-2.69 ± 2.55	10.8	-2.76 ± 2.66	10.8	-3.03 ± 2.89	10.8
128	-2.75 ± 2.61	10.8	-2.77 ± 2.63	10.8	-2.83 ± 2.70	10.8	-2.88 ± 2.73	10.8
256	-2.79 ± 2.64	10.8	-2.82 ± 2.67	10.8	-2.83 ± 2.69	10.8	-2.85 ± 2.70	10.8
N	$u_y(A) (\times 10^{-3})$	St_y	$u_y(A) (\times 10^{-3})$	St_y	$u_y(A) (\times 10^{-3})$	St_y	$u_y(A) (\times 10^{-3})$	St_y
32	1.47 ± 30.5	5.00	1.67 ± 32.4	5.00	1.56 ± 34.9	5.00	1.23 ± 36.1	5.42
64	1.41 ± 32.7	5.00	1.44 ± 33.4	5.00	1.41 ± 34.2	5.00	1.49 ± 35.3	5.00
128	1.42 ± 33.9	5.00	1.43 ± 34.0	5.00	1.44 ± 34.5	5.00	1.42 ± 34.7	5.00
256	1.42 ± 34.2	5.00	1.43 ± 34.3	5.00	1.42 ± 34.4	5.00	1.42 ± 34.5	5.00

Table 3: Results for the modified Turek-Hron benchmark using the three-point B-spline kernel with various values of M_{FAC} under different grid resolutions. N is the number of grid cells on coarsest grid level, $u_x(A)$ and $u_y(A)$ are x -, y -displacements of the point A , and St_x and St_y are Strouhal numbers for the oscillations of $u_x(A)$ and $u_y(A)$.

In this benchmark, we use an incompressible neo-Hookean material for the elastic beam, whose strain energy functional is defined as

$$W_{\text{NH}} = \frac{1}{2} \mu_s (\bar{I}_1 - 3), \quad (25)$$

in which μ_s is the shear modulus. We remark that this differs from the problem specification in that in Turek and Hron’s original paper, a compressible St. Venant-Kirchhoff model is used for the elastic beam, but our numerical framework enforces incompressibility on both solid and fluid by formulation, and so we cannot readily model the elastic beam as a compressible material. However, we also note that our results with an incompressible material model still are largely similar to the results from Turek and Hron using a compressible material model, which have a wide range of values reported in the literature. We do not expand on those results because that comparison is not the main focus of this study.

Table 3 shows comparisons for the three-point B-spline kernel for $M_{\text{FAC}} = 0.5, 1, 2$, and 4 under grid refinement. It reports the average and the amplitude of the x - and y -displacements ($u_x(A)$ and $u_y(A)$) of the point A , as well as the Strouhal numbers (St_x and St_y) to quantify the oscillations of $u_x(A)$ and $u_y(A)$. We obtain comparable results under grid refinement, which are more consistent between different M_{FAC} values as we refine the resolution. Similar to the results from other benchmarks, this benchmark also indicates that under grid refinement, the results become independent of M_{FAC} and the type of kernel. We again focus on the effect of M_{FAC} and the choice of kernel function at a relatively coarse resolution. Figures 11 and 12 compare representative kernels at $N = 64$ for $M_{\text{FAC}} = 0.5, 1, 2$, and 4 . The three-point B-spline kernel clearly yields more consistent results between different values of M_{FAC} at this Cartesian grid resolution. Table 4 summarizes the differences between selected kernels in Figures 11 and 12, and Appendix A provides the results for the remaining IB and B-spline kernels (see Figures S1 and S2), and Tables 4 and S1 show that the piecewise-linear and three-, four-, and five-point IB kernels report displacements that show large discrepancies from the converged displacements when we set $M_{\text{FAC}} = 0.5$. The six-point IB and three-, four-, five-, and six-point B-spline kernels produce displacements that are relatively consistent. However,

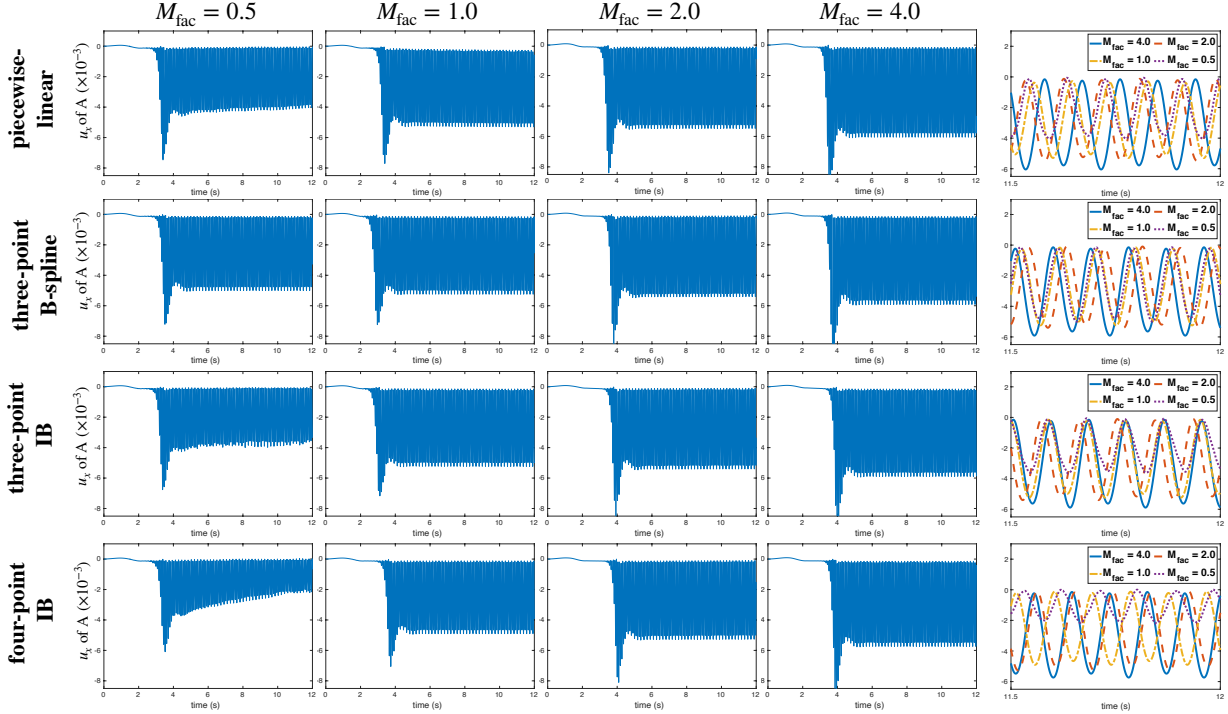


Figure 11: x -displacement (u_x) of the point A for different values of M_{FAC} for the modified Turek-Hron benchmark using different kernels at a Cartesian resolution of $N = 64$. Panels in the rightmost column show the periodic oscillations between $t = 11.5$ and $t = 12$.

	$M_{\text{FAC}} = 0.5$		$M_{\text{FAC}} = 1.0$		$M_{\text{FAC}} = 2.0$		$M_{\text{FAC}} = 4.0$	
Kernel	$u_x(A) (\times 10^{-3})$	St_x	$u_x(A) (\times 10^{-3})$	St_x	$u_x(A) (\times 10^{-3})$	St_x	$u_x(A) (\times 10^{-3})$	St_x
Piecewise-linear	-2.20 ± 2.14	10.4	-2.74 ± 2.53	10.8	-2.80 ± 2.68	10.4	-3.10 ± 2.95	10.8
B-spline (3-point)	-2.57 ± 2.44	10.8	-2.69 ± 2.55	10.8	-2.76 ± 2.66	10.8	-3.03 ± 2.89	10.8
IB (3-point)	-2.03 ± 1.97	10.4	-2.69 ± 2.54	10.4	-2.76 ± 2.65	10.8	-3.02 ± 2.87	10.8
IB (4-point)	-1.55 ± 1.56	10.4	-2.51 ± 2.39	10.4	-2.69 ± 2.58	10.8	-2.94 ± 2.80	10.8
Kernel	$u_y(A) (\times 10^{-3})$	St_y	$u_y(A) (\times 10^{-3})$	St_y	$u_y(A) (\times 10^{-3})$	St_y	$u_y(A) (\times 10^{-3})$	St_y
Piecewise-linear	1.38 ± 30.8	5.00	1.46 ± 33.2	5.00	1.45 ± 34.4	5.00	1.47 ± 35.9	5.00
B-spline (3-point)	1.41 ± 32.7	5.00	1.44 ± 33.4	5.00	1.41 ± 34.2	5.00	1.49 ± 35.3	5.00
IB (3-point)	1.37 ± 29.2	5.00	1.45 ± 33.3	5.00	1.42 ± 34.1	5.00	1.48 ± 35.2	5.00
IB (4-point)	1.04 ± 25.9	5.00	1.46 ± 32.2	5.00	1.41 ± 33.5	5.00	1.47 ± 34.6	5.00

Table 4: Results for the modified Turek-Hron benchmark using kernels in Figures 11 and 12. $N = 64$ is the number of grid cells on coarsest grid level, $u_x(A)$ and $u_y(A)$ are x -, y -displacements of the point A , and St_x and St_y are Strouhal numbers for the oscillations of $u_x(A)$ and $u_y(A)$.

Table 3 shows that the Strouhal numbers converge to 10.8, and only the three-point B-spline kernel shows the converged value for Strouhal number consistently for all values of $M_{\text{FAC}} = 0.5, 1, 2$, and 4 at a relatively coarse Cartesian resolution of $N = 64$. These results clearly demonstrate that the three-point B-spline kernel is less sensitive to changes in M_{FAC} , whereas other kernels show clear loss of accuracy as we refine the Lagrangian mesh for a fixed Eulerian grid that is relatively coarse.

3.4 Two-dimensional pressure-loaded elastic band

Results reported in Sections 3.1, 3.2, and 3.3 suggest that for any choice of kernel, larger M_{FAC} values generally give higher accuracy at a fixed Cartesian grid resolution. The tests considered so far, however, are examples of shear-dominant flows. Here we consider cases in which pressure loading dominates, as commonly

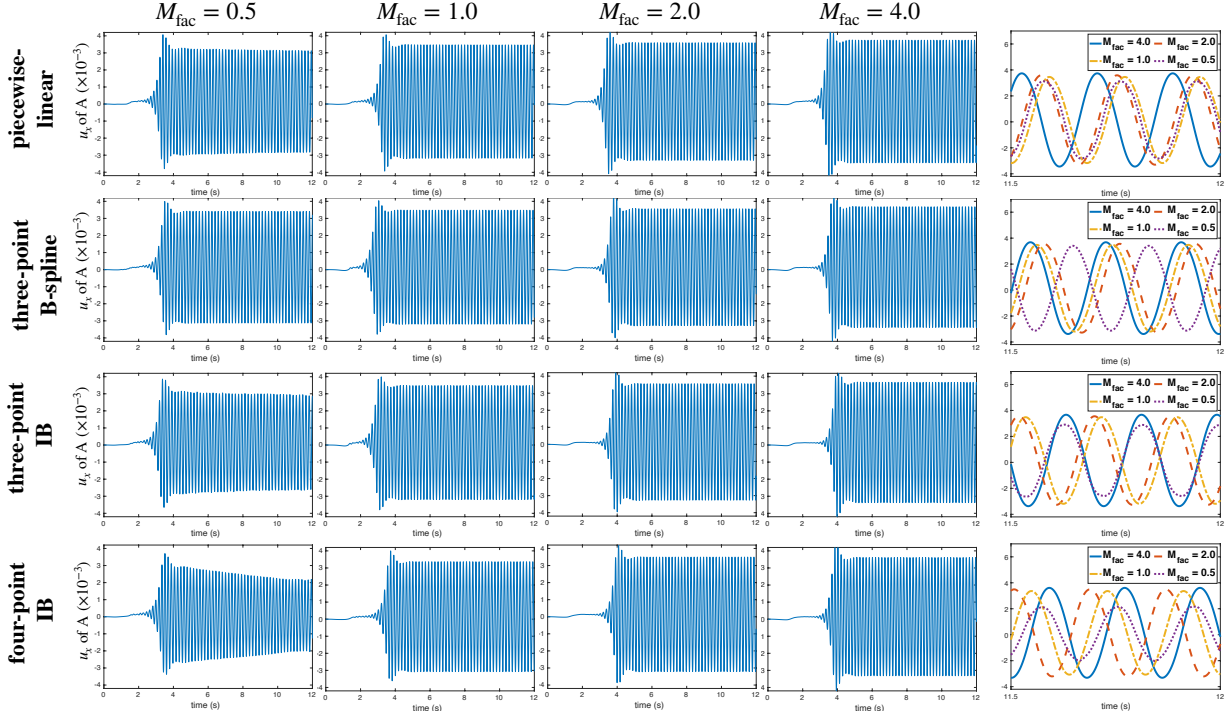


Figure 12: y -displacement (u_y) of the point A for different values of M_{FAC} for the modified Turek-Hron benchmark using different kernels at a Cartesian resolution of $N = 64$. Figures in the rightmost column show the periodic oscillations between $t = 11.5$ and $t = 12$.

	$M_{\text{FAC}} = 0.5$	$M_{\text{FAC}} = 0.75$	$M_{\text{FAC}} = 1.0$	$M_{\text{FAC}} = 2.0$	$M_{\text{FAC}} = 4.0$
L^2	3.3224×10^{-5}	6.4886×10^{-5}	1.6105×10^{-4}	6.5343×10^{-4}	1.6929×10^{-3}
L^∞	6.0554×10^{-4}	2.0530×10^{-3}	5.4120×10^{-3}	1.0623×10^{-2}	3.9397×10^{-2}

Table 5: Quantification of errors in velocity fields from the pressure-loaded two-dimensional elastic band for $M_{\text{FAC}} = 0.5, 0.75, 1, 2,$ and 4 shown in Figure 14. If the structural mesh is relatively coarser ($M_{\text{FAC}} > 1$) than the finest background Cartesian grids, then we obtain low accuracy for simulating pressurized elastic band.

encountered in biological and biomedical applications. To do so, we use a pressure-loaded “elastic band” model (Figure 13) that is adopted from Vadala-Roth et al. [34]. This uses an incompressible neo-Hookean material model as described in Section 3.3. We set $\rho = 1.0$ and $\mu = 0.01$. The computational domain is $2L \times L$, in which $L = 1$. The simulations use a uniform grid with an $2N \times N$ grid with $N = 128$. The fine-grid Cartesian cell size is $\Delta x = L/N$, and the time step size is $\Delta t = 0.001/N$. Fluid traction boundary conditions $\sigma(\mathbf{x}, t)\mathbf{n}(\mathbf{x}) = -5$ and $\sigma(\mathbf{x}, t)\mathbf{n}(\mathbf{x}) = 5$ are imposed on the left and right boundaries of the computational domain, respectively, and zero velocity is enforced along the top and bottom boundaries. The elastic band deforms and ultimately reaches a steady-state configuration determined by the pressure difference across the band. We use a grid resolution ($N = 128$) that is fine enough so that the elastic bands are well-resolved for all cases to isolate the effect of M_{FAC} on the Lagrangian-Eulerian coupling and eliminate the effect of elastic response from the band. Moreover, the effective shape of the kernel function changes near the boundary of the computational domain. So we avoid issues that may arise from using a finer structural mesh ($M_{\text{FAC}} = 0.5$) for the two rigid blocks by which the top and bottom of the band are fixed in place. In the continuous problem, there is no flow at equilibrium, but Figure 14 demonstrates that if the structural mesh is coarser than the finest background Cartesian grids ($M_{\text{FAC}} > 1$), apparent “leaks” develop. Table 5 confirms that the error is on the orders of magnitude larger with larger M_{FAC} values. Note that similar results are obtained with all of the kernels considered here.

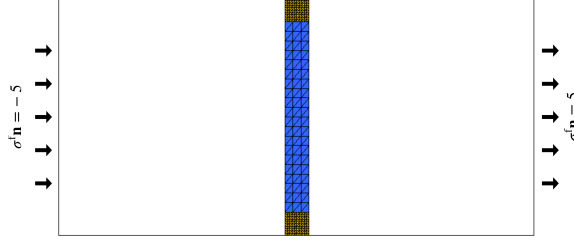


Figure 13: Schematic of two-dimensional pressure-loaded elastic band adopted from Vadala-Roth et al. [34]. The loading on the band (blue) is driven by fluid forces induced by the pressure gradient between the left and right boundaries of the computational domain. The effective shape of the kernel function changes near the boundary of the computational domain. So we avoid issues that may arise from using a finer structural mesh ($M_{\text{FAC}} = 0.5$) for the two rigid blocks (yellow) by which the top and bottom of the band are fixed in place. In this figure, $M_{\text{FAC}} = 2$ for the band away from the boundary.

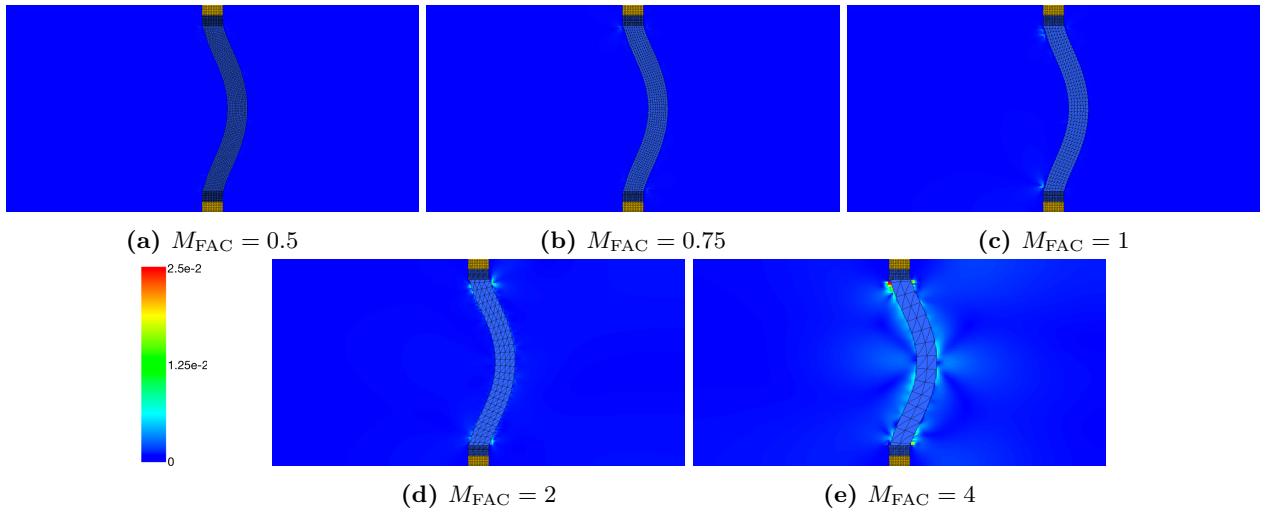


Figure 14: Comparison of velocity fields from the pressure-loaded two-dimensional elastic band for $M_{\text{FAC}} = 0.5, 0.75, 1, 2,$ and 4 . The simulations use an $N \times N$ grid with $N = 128$. The three-point B-spline kernel is used for this figure, but we observe the similar results with other kernels. If the structural mesh is relatively coarser ($M_{\text{FAC}} > 1$) than the finest background Cartesian grids, then we obtain low accuracy for simulating pressurized elastic band.

3.5 Bioprosthesis heart valve dynamics in a pulse duplicator

We aim to verify our key findings in a large-scale model. To do so, we consider an FSI model of bovine pericardial bioprosthesis heart valve (BHV) in a pulse duplicator, as described in detail by Lee et al. [15, 16]. The model includes a detailed IFED model of the aortic test section of an experimental pulse duplicator, and the simulation includes both substantial pressure-loads (during diastole, when the valve is closed) and shear-dominant flows (during systole, when the valve is open). The bovine pericardial valve leaflets are described by a modified version [15] of Holzapfel–Gasser–Ogden (HGO) model [53],

$$W_{\text{BHV}} = C_{10} \{ \exp [C_{01} (\bar{I}_1 - 3)] - 1 \} + \frac{k_1}{2k_2} \{ \exp [k_2 (\kappa \bar{I}_1 + (1 - 3\kappa) \bar{I}_4^* - 1)^2] - 1 \}, \quad (26)$$

in which $\bar{I}_4^* = \max(\bar{I}_4, 1) = \max(\mathbf{e}_0^T \bar{\mathbf{C}} \mathbf{e}_0, 1)$, and \mathbf{e}_0 is a unit vector aligned with the mean fiber direction in the reference configuration. The parameter $\kappa \in [0, \frac{1}{3}]$ describes collagen fiber angle dispersion. In the our simulations, we use $C_{10} = 0.119$ kPa, $C_{01} = 22.59$, $k_1 = 2.38$ MPa, $k_2 = 149.8$, and $\kappa = 0.292$ [15]. We use

$\rho = 1.0 \text{ g/cm}^3$ and $\mu = 1.0 \text{ cP}$. The computational domain is $5.05 \text{ cm} \times 10.1 \text{ cm} \times 5.05 \text{ cm}$. The simulations use a three-level locally refined grid with a refinement ratio of two between levels and an $N/2 \times N \times N/2$ coarse grid with $N = 64$, which yields a fine-grid Cartesian resolution of 0.4 mm. Three-element Windkessel (R–C–R) models establish the upstream driving and downstream loading conditions for the aortic test section. A combination of normal traction and zero tangential velocity boundary conditions are used at the inlet and outlet to couple the reduced-order models to the detailed description of the flow within the test section. Solid wall boundary conditions are imposed on the remaining boundaries of the computational domain. See Lee et al. [15] for further details.

Figures 15b and 15a compare cross-section views of velocity magnitude for the bovine BHV models for $M_{\text{FAC}} = 0.75$ and 1.5. It is clear in Figure 15b that there is significant leakage during diastole, whereas no leaks are apparent in Figure 15a. Figures 15c, 15d, and 15e compare simulated and experimental flow rates and pressure waveforms. The leaks that are evident in Figure 15b are also reflected in these measurements that the leaks are reflected in these measurements. Using $M_{\text{FAC}} = 0.75$, the flow rate and pressure data are in excellent agreement with those from the corresponding experiment, while we clearly observe leaks that are reflected as negative flow rate measurements. We also remark that the simulation using $M_{\text{FAC}} = 1.5$ is not able to proceed beyond $t \approx 0.25 \text{ s}$ without significantly reducing the time step size because of the high velocity concentrations observed in the regions highlighted in Figure 15b. The BHV leaflets in the $M_{\text{FAC}} = 1.5$ case also experience unphysical deformations at the free edges of the leaflets during systole.

4 Discussion

This study explores various choices of regularized delta functions to approximate the integral transforms (Eq. (3) and (4)) in the IFED method that could also apply more broadly to other IB methods. It also investigates the effect of relative structural mesh spacing for different kernels on the accuracy using standard FSI benchmark studies. A limitation of this study is that not all possible kernel function constructions are considered. Another limitation is that it considers specific Lagrangian and Eulerian spatial discretizations. The impact of the choice of regularized delta function or relative mesh spacing could depend on these discretizations. For instance, different Lagrangian-Eulerian coupling strategies, such as node-based approximations to the integral transforms, may not be suitable for use with $M_{\text{FAC}} > 1$. The benchmark results indicate that in general the kernels satisfying the even-odd condition require higher resolution to achieve similar accuracy as kernels that do not satisfy this condition, which may suggest that the even-odd condition induces mild instabilities that are not present for kernels that do not satisfy this condition. We also demonstrate that narrower kernels, such as the three-point B-spline kernel, yield higher accuracies for a given resolution. A possible explanation could be that the kernels with larger support results in larger numerical boundary layers. The results in Sections 3.1, 3.2, and 3.3 indicate that we obtain improved accuracy with a given Cartesian grid resolution for these shear-dominant cases by using relatively coarser Lagrangian nodal spacing ($M_{\text{FAC}} > 1$). However, in the pressure-loaded case considered in Section 3.4, we observe that the Lagrangian mesh needs to be similar or relatively finer compared to the Cartesian grids ($M_{\text{FAC}} \leq 1$) to avoid leaks. In fact, it is common in simulations using complex geometries to have many mesh elements that are similar or even relatively finer compared to the background Cartesian grid to preserve fine geometric features. Understanding this transition in accuracy between shear-dominant and pressure-loaded cases is a possible future area of research. These results together suggest that the three-point B-spline kernel is relatively less sensitive to the relative mesh spacing with respect to the Eulerian grid spacing.

We then apply our findings from benchmark studies with an FSI model of bovine pericardial BHV in a pulse duplicator, which involves both pressure-loaded and shear-dominant flows in a rigid and stationary channel with immersed elastic structures inside. We confirm that these results are consistent with our findings from benchmark studies and that we obtain accurate results only for $M_{\text{FAC}} \leq 1$. The benchmarks show that the three-point B-spline kernel is the best overall choice considering both shear- and pressure-dominant flows because it is less sensitive to the relative structural mesh spacing. We note that under sufficiently fine grid resolution, different kernels appear to converge to the same results. However, this study suggests that optimal numerical settings will provide consistent solution under relatively coarse grid resolutions that facilitate the deployment of the methodology to complex, large-scale three-dimensional models. Although this study is done within the context of the IFED method, the effect of different kernels could be important

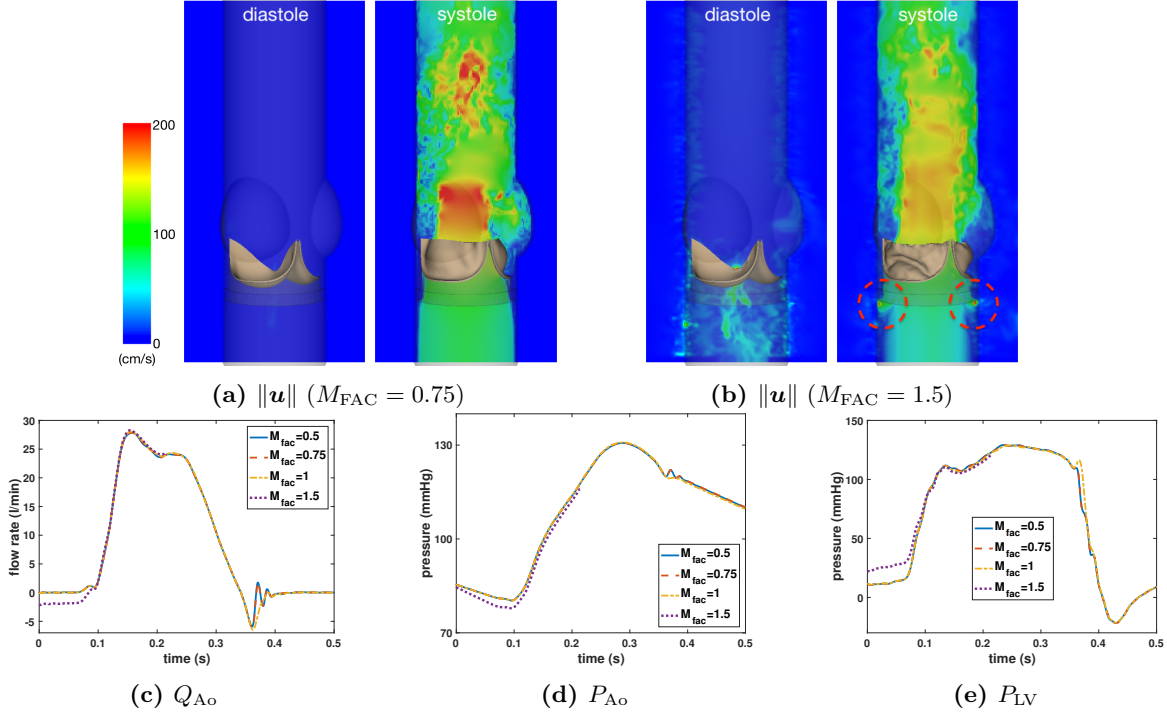


Figure 15: Representative comparison of cross-section views of simulated velocity magnitudes for the bovine pericardial valve models for (a) $M_{FAC} = 0.75$ and (b) 1.5 during diastole (pressure-loaded when the valve is closed) and systole (shear-dominant flow when the valve is open). The simulations use a three-level locally refined grid with a refinement ratio of two between levels and an $N/2 \times N \times N/2$ coarse grid with $N = 64$, which corresponds to $N = 256$ at the finest level. We also look at comparisons of (c) flow rates (Q_{Ao}), (d) downstream pressure (P_{Ao}), and (e) upstream pressure (P_{LV}) waveforms measured from simulations with $M_{FAC} = 0.5, 0.75, 1, 1.5$. In panel (b) we see flow leaks during diastole as well as local regions with unphysical velocity concentrations during systole (red dashed circles). All comparisons in panels (c)-(e) also indicate that $M_{FAC} = 0.5, 0.75,$ and 1 are in excellent agreement. However, we clearly observe leaks in (b) with $M_{FAC} = 1.5$, which are reflected as negative flow rate measurement as shown in (c). As a result, we also observe discrepancies in both downstream and upstream pressure for $M_{FAC} = 1.5$.

not just for this method, but also for other IB-type methods more generally.

Acknowledgments

J.H.L. acknowledges funding from the NIH Integrative Vascular Biology Training Fellowship (Award 5T32HL069768-17) at the University of North Carolina School of Medicine. B.E.G. acknowledges funding from the NIH (Awards R01HL117063 and U01HL143336) and NSF (Awards OAC 1450327, OAC 1652541, OAC 1931516, and CBET 1757193). Simulations were performed using facilities provided by the University of North Carolina at Chapel Hill through the Research Computing Division of UNC Information Technology Services. We thank Aaron Barrett, Ebrahim M. Kolahdouz, Ben Vadala-Roth, and David Wells for their constructive comments in improving the manuscript.

Conflict of Interest

No conflict of interest.

References

- [1] C. S. Peskin, The immersed boundary method, *Acta Numer* 11 (2002) 479–517.
- [2] C. S. Peskin, Flow patterns around heart valves: a numerical method, *J Comput Phys* 10 (2) (1972) 252–271.
- [3] C. S. Peskin, Numerical analysis of blood flow in the heart, *J Comput Phys* 25 (3) (1977) 220–252.
- [4] B. E. Griffith, X. Y. Luo, Hybrid finite difference/finite element immersed boundary method, *Int J Numer Methods Biomed Eng* 33 (11) (2017) e2888.
- [5] B. E. Griffith, N. A. Patankar, Immersed method for fluid–structure interaction, *Annu Rev Fluid Mech* 52 (2020) 421–448.
- [6] B. E. Griffith, X. Y. Luo, D. M. McQueen, C. S. Peskin, Simulating the fluid dynamics of natural and prosthetic heart valves using the immersed boundary method, *Int J Appl Mech* 1 (1) (2009) 137–177.
- [7] B. E. Griffith, Immersed boundary model of physiological driving and loading conditions, *Int J Numer Methods Biomed Eng* 28 (3) (2012) 317–345.
- [8] X. Y. Luo, B. E. Griffith, X. S. Wang, M. Yin, T. J. Wang, C. L. Liang, P. N. Watton, G. M. Bernacca, Effect of bending rigidity in a dynamic model of a polyurethane prosthetic mitral valve, *Biomech Model Mechanobiol* 11 (6) (2012) 815–827.
- [9] H. Gao, D. Carrick, C. Berry, B. E. Griffith, X. Y. Luo, Dynamic and finite-strain modelling of the human left ventricle in health and disease using an immersed boundary-finite element method, *IMA J Appl Math* 79 (5) (2014) 978–1010.
- [10] V. Flamini, A. DeAnda, B. E. Griffith, Immersed boundary-finite element model of fluid–structure interaction in the aortic root, *Theor Comput Fluid Dyn* 30 (1) (2016) 139–164.
- [11] W. W. Chen, H. Gao, X. Y. Luo, N. A. Hill, Study of cardiovascular function using a coupled left ventricle and systemic circulation model, *J Biomech* 49 (12) (2016) 2445–2454.
- [12] H. Gao, L. Feng, N. Qi, C. Berry, B. E. Griffith, X. Y. Luo, A coupled mitral valve-left ventricle model with fluid-structure interaction, *Med Eng Phys* 47 (2017) 128–136.
- [13] A. Hasan, E. M. Kolahdouz, A. Enquobahrie, T. G. Caranasos, J. P. Vavalle, B. E. Griffith, Image-based immersed boundary model of the aortic root, *Med Eng Phys* 47 (2017) 72–84.
- [14] L. Feng, N. Qi, H. Gao, W. Sun, M. Vazquez, B. E. Griffith, X. Y. Luo, On the chordae structure and dynamic behaviour of the mitral valve, *IMA J Appl Math* 83 (6) (2018) 1066–1091.
- [15] J. H. Lee, A. D. Rygg, E. M. Kolahdouz, S. Rossi, S. M. Retta, N. Duraiswamy, L. N. Scotten, B. A. Craven, B. E. Griffith, Fluid–structure interaction models of bioprosthetic heart valve dynamics in an experimental pulse duplicator, *Ann Biomed Eng* 48 (5) (2020) 1475–1490.
- [16] J. H. Lee, L. N. Scotten, R. Hunt, T. G. Caranasos, J. P. Vavalle, B. E. Griffith, Bioprosthetic aortic valve diameter and thickness are directly related to leaflet fluttering: Results from a combined experimental and computational modeling study, *J Thorac Cardiovasc Surg Open*.
- [17] T. Skorczewski, B. E. Griffith, A. L. Fogelson, *Biological Fluid Dynamics: Modeling, Computations, and Applications*, Vol. 628 of *Contemporary Mathematics*, American Mathematical Society, 2014, Ch. Multi-bond models for platelet adhesion and cohesion, pp. 149–172.
- [18] W. Kou, A. P. S. Bhalla, B. E. Griffith, J. E. Pandolfino, P. J. Kahrilas, N. A. Patankar, A fully resolved active musculo-mechanical model for esophageal transport, *J Comput Phys* 298 (2015) 446–465.
- [19] W. Kou, B. E. Griffith, J. E. Pandolfino, P. J. Kahrilas, N. A. Patankar, A continuum mechanics-based musculo-mechanical model for esophageal transport, *J Comput Phys* 348 (2017) 433–459.

- [20] W. Kou, J. E. Pandolfino, P. J. Kahrilas, N. A. Patankar, Studies of abnormalities of the lower esophageal sphincter during esophageal emptying based on a fully-coupled bolus-esophageal-gastric model, *Biomech Model Mechanobiol* 17 (4) (2018) 1069–1082.
- [21] N. A. Battista, A. N. Lane, J. Liu, L. A. Miller, Fluid dynamics of heart development: Effects of trabeculae and hematocrit, *Math Med Biol* 35 (4) (2018) 493–516.
- [22] S. K. Jones, R. Laurenza, T. L. Hedrick, B. E. Griffith, L. A. Miller, Life vs. drag based mechanisms for vertical force production in the smallest flying insects, *J Theor Biol* 384 (2015) 105–120.
- [23] A. Santhanakrishnan, S. Jones, W. Dickson, M. Peek, V. Kasoju, M. Dickinson, L. Miller, Flow structure and force generation on flapping wings at low Reynolds numbers relevant to the flight of tiny insects, *Fluids* 3 (3) (2018) 45.
- [24] S. Alben, L. A. Miller, J. Peng, Efficient kinematics for jet-propelled swimming, *J Fluid Mech* 733 (2013) 100–133.
- [25] A. P. S. Bhalla, R. Bale, B. E. Griffith, N. A. Patankar, Fully resolved immersed electrohydrodynamics for particle motion, electrolocation, and self-propulsion, *J Comput Phys* 256 (2014) 88–108.
- [26] E. D. Tytell, C. Hsu, L. J. Fauci, The role of mechanical resonance in the neural control of swimming in fishes, *Zoology* 117 (1) (2014) 48–56.
- [27] R. Bale, A. P. S. Bhalla, I. D. Neveln, M. A. MacIver, N. A. Patankar, Convergent evolution of mechanically optimal locomotion in aquatic invertebrates and vertebrates, *PLoS Biol* 3 (4) (2015) e1002123.
- [28] A. P. Hoover, B. E. Griffith, L. A. Miller, Quantifying performance in the medusan mechanospace with an actively swimming three-dimensional jellyfish model, *J Fluid Mech* 813 (2017) 1112–1155.
- [29] N. Nangia, R. Bale, N. Chen, Y. Hanna, N. A. Patankar, Optimal specific wavelength for maximum thrust production in undulatory propulsion, *PLoS ONE* 12 (6) (2017) e0179727.
- [30] A. M. Roma, C. S. Peskin, M. J. Berger, An adaptive version of the immersed boundary method, *J Comput Phys* 153 (2) (1999) 509–534.
- [31] Y. Liu, Y. Mori, Properties of discrete delta functions and convergence of the immersed boundary method, *SIAM J Numer Anal* 50 (6) (2012) 2986–3015.
- [32] Y. Bao, J. Kaye, C. S. Peskin, A Gaussian-like immersed-boundary kernel with three continuous derivatives and improved translational invariance, *J Comput Phys* 316 (2016) 139–144.
- [33] Y. Bao, A. Donev, B. E. Griffith, D. M. McQueen, C. S. Peskin, An immersed boundary method with divergence-free velocity interpolation and force spreading, *J Comput Phys* 347 (2017) 183–206.
- [34] B. Vadala-Roth, S. Acharya, N. A. Patankar, S. Rossi, B. E. Griffith, Stabilization approaches for the hyperelastic immersed boundary method for problems of large-deformation incompressible elasticity, *Comput Methods Appl Mech Eng* 365 (2020) 112978.
- [35] D. Goldstein, R. Handler, L. Sirovich, Modeling a no-slip flow boundary with an external force field, *J Comput Phys* 105 (2) (1993) 354–366.
- [36] L. Zhang, A. Gerstenberger, X. Wang, W. K. Liu, Immersed finite element method, *Comput Methods Appl Mech Engrg* 193 (21–22) (2004) 2051–2067.
- [37] L. T. Zhang, M. Gay, Immersed finite element method for fluid-structure interactions, *J Fluids Struct* 23 (6) (2007) 839–857.
- [38] X. Wang, C. Wang, L. T. Zhang, Semi-implicit formulation of the immersed finite element method, *Comput Methods Appl Mech Engrg* 49 (4) (2012) 421–430.

- [39] D. Boffi, L. Gastaldi, L. Heltai, C. S. Peskin, On the hyper-elastic formulation of the immersed boundary method, *Comput Methods Appl Mech Eng* 197 (25–28) (2008) 2210–2231.
- [40] B. E. Griffith, An accurate and efficient method for the incompressible Navier–Stokes equations using the projection method as a preconditioner, *J Comput Phys* 228 (20) (2009) 7565–7595.
- [41] B. E. Griffith, On the volume conservation of the immersed boundary method, *Commun Comput Phys* 12 (2) (2012) 401–432.
- [42] P. Colella, P. R. Woodward, The piecewise parabolic method (PPM) for gas-dynamical simulations, *J Comput Phys* 54 (1) (1984) 174–201.
- [43] M. Unser, A. Aldroubi, M. Eden, On the asymptotic convergence of B-spline wavelets to Gabor functions, *IEEE Trans Inf Theory* 38 (2) (1992) 864–872.
- [44] C. Sansour, On the physical assumptions underlying the volumetric-isochoric split and the case of anisotropy, *Eur J Mech A/Solids* 27 (2008) 28–39.
- [45] C. H. Liu, G. Hofstetter, H. A. Mang, 3d finite element analysis of rubber-like materials at finite strains, *Eng Comput* 11 (2) (1994) 111–128.
- [46] B. E. Griffith, R. D. Hornung, D. M. McQueen, C. S. Peskin, An adaptive, formally second order accurate version of the immersed boundary method, *J Comput Phys* 223 (1) (2007) 10–49.
- [47] IBAMR: Immersed Boundary Method Adaptive Mesh Refinement Software Infrastructure. <https://ibamr.github.io/>.
URL <https://ibamr.github.io/>
- [48] R. D. Hornung, S. R. Kohn, Managing application complexity in the SAMRAI object-oriented framework, *Concurr Comput Pract Exp* 14 (2002) 347–368.
- [49] B. S. Kirk, J. W. Peterson, R. H. Stogner, G. F. Carey, **libMesh**: a C++ library for parallel adaptive mesh refinement/coarsening simulations, *Eng Comput* 22 (3–4) (2006) 237–254.
- [50] S. Balay, S. Abhyankar, M. F. Adams, J. Brown, P. Brune, K. Buschelman, L. Dalcin, A. Dener, V. Eijkhout, W. D. Gropp, D. Karpeyev, D. Kaushik, M. G. Knepley, D. A. May, L. C. McInnes, R. T. Mills, T. Munson, K. Rupp, P. Sanan, B. F. Smith, S. Zampini, H. Zhang, H. Zhang, *PETSc Users Manual*, Tech. Rep. ANL-95/11 - Revision 3.15, Argonne National Laboratory (2021).
URL <http://www.mcs.anl.gov/petsc>
- [51] K. Taira, T. Colonius, The immersed boundary method: a projection approach, *J Comput Phys* 225 (2) (2007) 2118–2137.
- [52] S. Turek, J. Hron, Proposal for numerical benchmarking of fluid–structure interaction between an elastic object and laminar incompressible flow, in: H. J. Bungartz, M. Schäfer (Eds.), *Fluid–Structure Interaction*, Vol. 53 of *Lecture Notes in Computational Science and Engineering*, Springer, Berlin, Heidelberg, 2006, pp. 371–385.
- [53] T. C. Gasser, R. W. Ogden, G. A. Holzapfel, Hyperelastic modelling of arterial layers with distributed collagen fibre orientations, *J R Soc Interface* 3 (6) (2006) 15–35.

Kernel	$M_{\text{FAC}} = 0.5$		$M_{\text{FAC}} = 1.0$		$M_{\text{FAC}} = 2.0$		$M_{\text{FAC}} = 4.0$	
	$u_x(A) (\times 10^{-3})$	St_x	$u_x(A) (\times 10^{-3})$	St_x	$u_x(A) (\times 10^{-3})$	St_x	$u_x(A) (\times 10^{-3})$	St_x
IB (3-point)	-2.03 ± 1.97	10.4	-2.69 ± 2.54	10.4	-2.76 ± 2.65	10.8	-3.02 ± 2.87	10.8
IB (4-point)	-1.55 ± 1.56	10.4	-2.51 ± 2.39	10.4	-2.69 ± 2.58	10.8	-2.94 ± 2.80	10.8
IB (5-point)	-2.51 ± 2.38	10.4	-2.57 ± 2.44	10.4	-2.70 ± 2.60	10.8	-2.95 ± 2.81	10.8
IB (6-point)	-2.46 ± 2.35	10.4	-2.48 ± 2.36	10.4	-2.65 ± 2.53	10.4	-2.89 ± 2.75	10.8
B-spline (3-point)	-2.57 ± 2.44	10.8	-2.69 ± 2.55	10.8	-2.76 ± 2.66	10.8	-3.03 ± 2.89	10.8
B-spline (4-point)	-2.53 ± 2.42	10.4	-2.67 ± 2.54	10.4	-2.74 ± 2.63	10.8	-3.00 ± 2.86	10.8
B-spline (5-point)	-2.55 ± 2.43	10.4	-2.63 ± 2.50	10.8	-2.72 ± 2.62	10.8	-2.98 ± 2.84	10.8
B-spline (6-point)	-2.54 ± 2.42	10.4	-2.58 ± 2.46	10.4	-2.70 ± 2.60	10.8	-2.96 ± 2.82	10.8

Kernel	$u_y(A) (\times 10^{-3})$		$u_y(A) (\times 10^{-3})$		$u_y(A) (\times 10^{-3})$		$u_y(A) (\times 10^{-3})$	
	$u_y(A) (\times 10^{-3})$	St_y	$u_y(A) (\times 10^{-3})$	St_y	$u_y(A) (\times 10^{-3})$	St_y	$u_y(A) (\times 10^{-3})$	St_y
IB (3-point)	1.37 ± 29.2	5.00	1.45 ± 33.3	5.00	1.42 ± 34.1	5.00	1.48 ± 35.2	5.00
IB (4-point)	1.04 ± 25.9	5.00	1.46 ± 32.2	5.00	1.41 ± 33.5	5.00	1.47 ± 34.6	5.00
IB (5-point)	1.39 ± 32.2	5.00	1.48 ± 32.6	5.00	1.41 ± 33.6	5.00	1.48 ± 34.7	5.00
IB (6-point)	1.39 ± 31.9	5.00	1.44 ± 32.0	5.00	1.41 ± 33.2	5.00	1.47 ± 34.3	5.00
B-spline (3-point)	1.41 ± 32.7	5.00	1.44 ± 33.4	5.00	1.41 ± 34.2	5.00	1.49 ± 35.3	5.00
B-spline (4-point)	1.41 ± 32.5	5.00	1.46 ± 33.3	5.00	1.42 ± 34.0	5.00	1.48 ± 35.1	5.00
B-spline (5-point)	1.39 ± 32.5	5.00	1.48 ± 33.0	5.00	1.42 ± 33.8	5.00	1.48 ± 34.9	5.00
B-spline (6-point)	1.41 ± 32.4	5.00	1.48 ± 32.6	5.00	1.41 ± 33.7	5.00	1.48 ± 34.8	5.00

Table S1: Results for the modified Turek-Hron benchmark with different IB and B-spline kernels and various values of M_{FAC} at a Cartesian resolution of $N = 64$.

Appendix

A Turek-Hron Benchmark Results for Various Choices of Kernel Function

This section details results for the modified Turek-Hron benchmark using various IB and B-spline kernels (see Figures S1 and S2). Table S1 reports the means for $u_x(A)$ and $u_y(A)$, which are x -, y -displacements of the point A , as well as the Strouhal numbers corresponding to the oscillations of $u_x(A)$ and $u_y(A)$ at periodic steady-state. Here we look at relatively coarser resolution cases, in which the number of grid cells on coarsest grid level is $N = 64$. These results indicate that the three-point B-spline kernel is the only kernel that shows consistent Strouhal numbers for all values of $M_{\text{FAC}} = 0.5, 1, 2, \text{ and } 4$ at $N = 64$, and that it is less sensitive to changes in M_{FAC} . Other kernels show loss of accuracy as we refine the Lagrangian mesh for a fixed Eulerian grid that is relatively coarse.

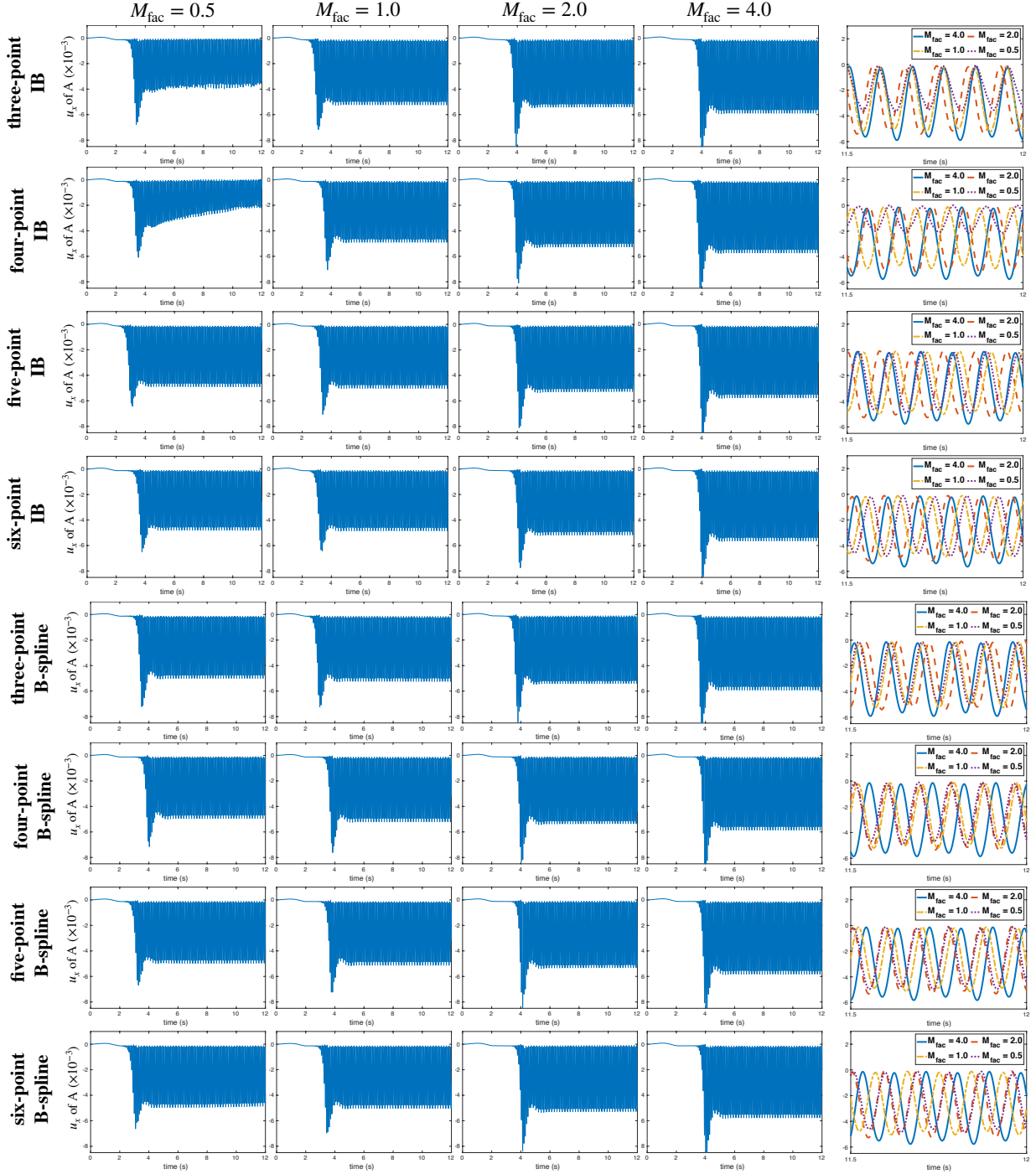


Figure S1: x -displacement (u_x) of the point A for different values of M_{FAC} for the modified Turek-Hron benchmark using different IB and B-spline kernels at a Cartesian resolution of $N = 64$. Figures in the rightmost panels show the periodic oscillations between $t = 11.5$ and $t = 12$.

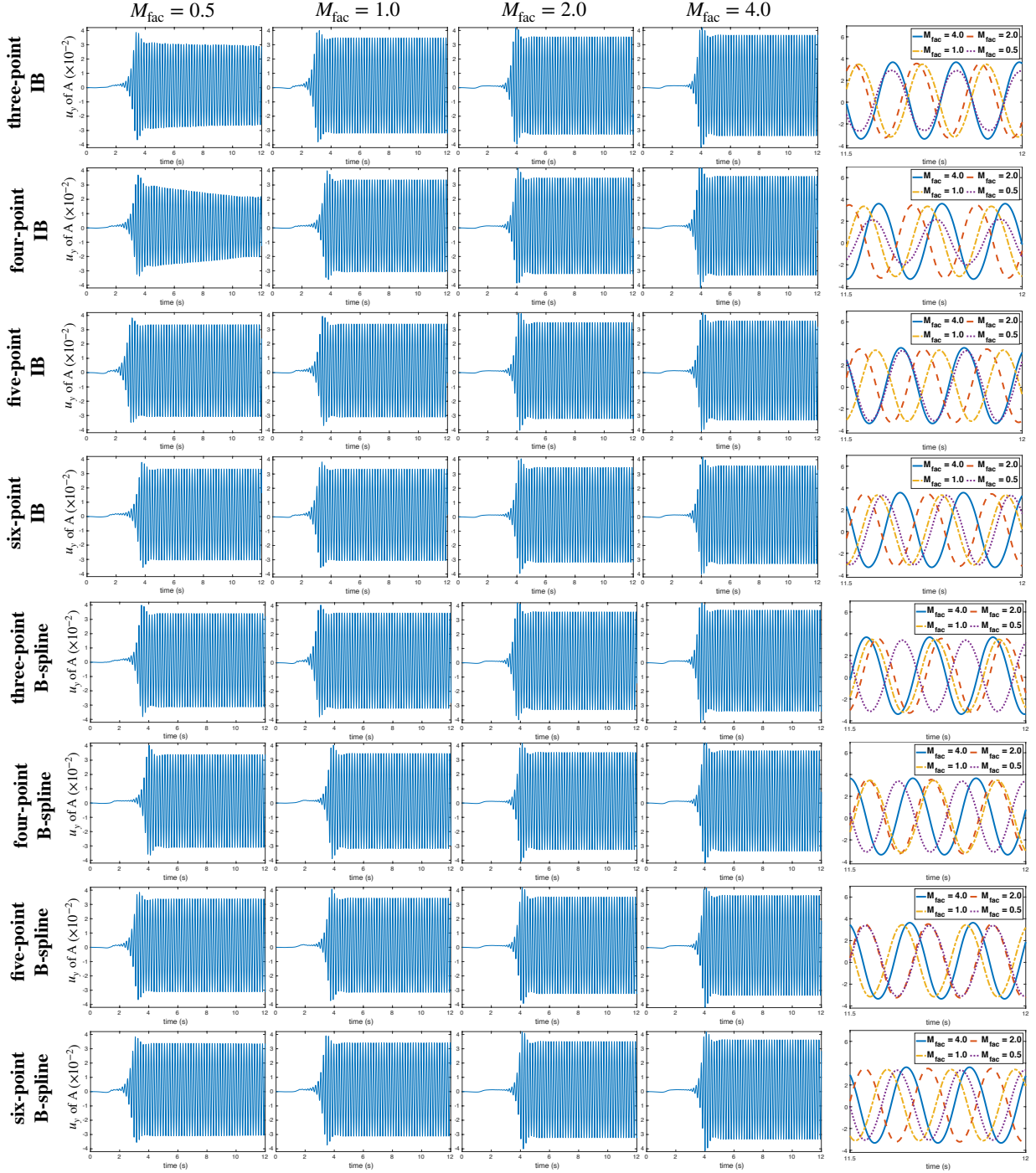


Figure S2: y -displacement (u_y) of the point A for different values of M_{FAC} for the modified Turek-Hron benchmark using different IB and B-spline kernels at a Cartesian resolution of $N = 64$. Figures in the rightmost panels show the periodic oscillations between $t = 11.5$ and $t = 12$.